

Steady advection-diffusion around finite absorbers in two-dimensional potential flows

By JAEHYUK CHOI¹, DIONISIOS MARGETIS¹,
TODD M. SQUIRES², AND MARTIN Z. BAZANT¹

¹Department of Mathematics

Massachusetts Institute of Technology, Cambridge, MA 02139

²Departments of Applied and Computational Mathematics and Physics,
California Institute of Technology, Pasadena, CA 91125

(Received 3 March 2019)

We perform an exhaustive study of the simplest, nontrivial problem in advection-diffusion: a finite absorber of arbitrary cross section in a steady two-dimensional potential flow of concentrated fluid. This classical problem has been studied extensively in the theory of solidification from a flowing melt, and it also arises in Advection-Diffusion-Limited Aggregation. In both cases, the fundamental object is the flux to a circular disk, obtained by conformal mapping from more complicated shapes. We construct the first accurate numerical solution using an efficient new method, which involves mapping to the interior of the disk and using a spectral method in polar coordinates. Our method also combines exact asymptotics and an adaptive mesh to handle boundary layers. Starting from a well-known integral equation in stream line coordinates, we also derive new, high-order asymptotic expansions for high and low Peclet numbers (Pe). Remarkably, the high- Pe expansion remains accurate even for such low Pe as 10^{-3} . The two expansions overlap well near $Pe = 0.1$, allowing the construction of an analytical connection formula that is uniformly accurate for all Pe and angles on the disk with a maximum relative error of 1.75%. We also obtain an analytical formula for the Nusselt number (Nu) as a function of the Peclet number with a maximum relative error of 0.53% for all possible geometries. Because our finite-plate problem can be conformally mapped to other geometries, the general problem of two-dimensional convection-diffusion past an arbitrary finite absorber in a potential flow can be considered effectively solved.

1. Introduction

The transfer of mass, heat, or other passive scalars in fluid flows is a major theme in transport science (Leal 1992). The canonical model problem involves a uniform background flow of speed, U_1 , and concentration, C_1 , past an absorbing object of characteristic size, L . Given the steady, incompressible flow field, u (scaled to U_1), the steady tracer concentration around the object, c (scaled to C_1), satisfies the (dimensionless) linear advection-diffusion equation,

$$Pe_0 u \cdot \nabla c = \nabla^2 c \quad (1.1)$$

where $Pe_0 = U_1 L/D$ is the bare Peclet number, which measures the relative importance of advection compared to diffusion (with a diffusivity, D). This partial differential equation (PDE) must be solved subject to the boundary conditions (BC), $c = 0$ on the object

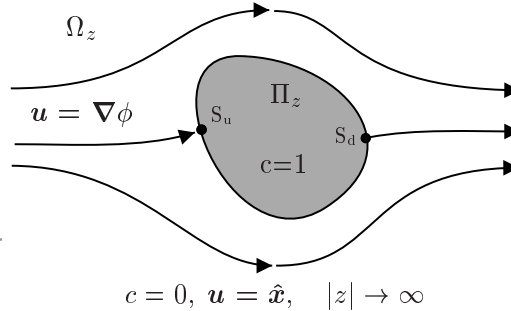


Figure 1. The fundamental problem of advection-diffusion: A finite absorber (source) in a steady flow of uniformly concentrated (depleted) fluid in the complex z plane; Ω_z is the region occupied by the object, and Π_z is its exterior.

and $c = 1$ far away (at l), to obtain the dimensionless normal flux density,

$$= \hat{n} \cdot \mathbf{r} c; \quad (1.2)$$

everywhere on the surface of the object. (Since the problem is linear, we may also consider the equivalent problem of a source object at $c = 1$ relative to a depleted background fluid at $c = 0$.)

Although similarity solutions exist for infinite leading edges (see below), in the usual case of a finite absorber, the mathematical problem is intractable. It can even be difficult to solve numerically because Pe_δ appears as a singular perturbation in the PDE in both limits, $Pe_\delta \gg 1$ and $Pe_\delta \ll 0$. The classical approach, therefore, has been to employ asymptotic analysis to obtain approximate solutions, usually relating the total integrated flux, or Nusselt number, Nu , to the Péclet number, Pe . Early studies of this type focused on spheres (Arcivos & Taylor, 1962) and more complicated shapes (Brenner, 1963) in Stokes flows. Related work continues to the present day, e.g. in the context of nutrient uptake by single-cell organisms (Magar et al., 2003).

The $Nu(Pe)$ relation contains useful global information, but one often requires a complete solution to the problem, including the local flux profile on the absorber. In this paper, we focus on a well known special case, ideally suited for mathematical analysis: steady advection-diffusion in a two-dimensional potential flow. The dimensionless boundary-value problem (BVP) is:

$$Pe_\delta \mathbf{r} \cdot \mathbf{r} c = \nabla^2 c; \quad \mathbf{r}^2 = 0; \quad (\mathbf{x}; \mathbf{y}) \in \partial_z \quad (1.3)$$

$$c = 1; \quad \hat{n} \cdot \mathbf{r} = 0; \quad (\mathbf{x}; \mathbf{y}) \in \partial_z \text{ and } c \neq 0; \quad x^2 + y^2 \ll 1; \quad (1.4)$$

$$\mathbf{r} \cdot \hat{\mathbf{x}}; \quad x^2 + y^2 \ll 1; \quad (1.5)$$

where ∂_z is the flow region, exterior to the absorbing boundary, ∂_z , as shown in Figure 1.

The key to analyzing (1.3) is to view points in the plane as complex numbers, $z = x + iy$. For example, this enables a transformation to streamline coordinates, $\zeta = \psi + i\phi$, which reduces the problem to a thin absorbing strip in a uniform flow (Boussinesq, 1905). For a more general perspective in terms of conformal mapping, see Bazant (2004). Using complex-variable techniques, the general system of PDEs (1.3) has been studied recently with applications to tracer dispersion (Koplik et al., 1994) and heat transfer (Morgan & Bejan, 1994) in porous media, as well as vorticity diffusion in strained wakes (Eames & Bush, 1999; Hunt & Eames, 2002).

Complex analysis becomes particularly useful when the interface, $\partial_z(t)$, is a moving free boundary, driven by the local flux density, $\mathbf{r} \cdot \hat{\mathbf{n}}$. For a broad class of transport-

limited growth phenomena, the interfacial dynamics, whether deterministic or stochastic, can be formulated in terms of a time-dependent conformal map from a simple, static domain to the evolving, physical domain (Bazant et al., 2003). For continuous growth by advection-diffusion, this approach was introduced by Wijngaarden (1966) and Maksimov (1976), who solved (1.3)-(1.5) in stream line coordinates. Maksimov's method has been used extensively by Komev and his collaborators to describe solidification and freezing from a flowing melt (Chugunov & Komev, 1986; Komev & Chugunov, 1988; Komev & Mukhamadullina, 1994; Alimov et al., 1994; Alimov et al., 1998; Cummings & Komev, 1999; Cummings et al., 1999). These studies significantly extend the conformal map dynamics for Laplacian growth by pure diffusion, without advection (Polubarinova-Kochina 1945; Galin, 1945; Howison, 1992).

Here, we are motivated by a new, discrete growth model, Advection-Diffusion-Limited Aggregation (ADLA), which describes the growth of fractal aggregates in a fluid flow via a stochastic conformal map (Bazant et al., 2003). In that case, the boundary value problem (1.3) must be solved for a circular absorber for all values of Pe_0 . The normal flux distribution, $\phi_z(\cdot; Pe_0)$, determines the probability measure for growth events. The detailed description of the growth measure in this paper shows how dynamics crosses over from diffusion-dominated to advection-dominated growth regimes, as a function of the time-dependent Peclet number. These two "fixed points" of the dynamics are related to special similarity solutions (Bazant, 2004), which correspond to the asymptotic regimes of high and low Pe_0 analyzed in this paper.

Beyond such applications, the BVP (1.3)-(1.5), for an arbitrary single-connected domain, Ω , merits serious mathematical study in its own right. It is perhaps the simplest advection-diffusion problem with a nontrivial dependence on the Peclet number. It may also be the most complicated advection-diffusion problem for which a nearly exact analytical solution is possible, as we show here for the first time.

The paper is organized as follows. In Sec. 2 we set the stage for our analysis by reviewing two key properties of the BVP (1.3)-(1.5): (i) It can be recast as a singular integrodifferential equation in stream line coordinates, and (ii) conformal mapping can be applied to work in other convenient geometries for numerical solution and mathematical analysis. In Sec. 3, we present an efficient, new numerical method to solve the BVP, after conformal mapping to the interior of a circular disk. In Sec. 4, we derive accurate asymptotic expansions for ϕ_z for high Peclet numbers by applying an exact iterative procedure to the integral equation. In Sec. 5 approximate formulae for ϕ_z are derived when Pe is sufficiently small via approximating the kernel of the integral equation and solving the resulting equation exactly by known methods. In Sec. 6 an accurate ad hoc connection formula is given for ϕ_z by combining the formulae for high and low Pe , and it is also integrated to obtain the $Nu(Pe)$ relation. Finally, in Sec. 7 we conclude with a discussion of some of the implications and applications of our results, as well as by posing a few challenges for future work.

2. Mathematical Preliminaries

2.1. Stream line Coordinates

In his analysis of high Reynolds number flows, Boussinesq (1905) discovered a hodograph transformation (exchanging dependent and independent variables) which greatly simplifies (1.3). It is well known that the velocity potential is the real part of an analytic complex potential, $\phi = \phi + i\psi$, where the harmonic conjugate, ψ , is the stream function (Batchelor 1967). Using the Cauchy-Riemann equations, it is easy to show that the

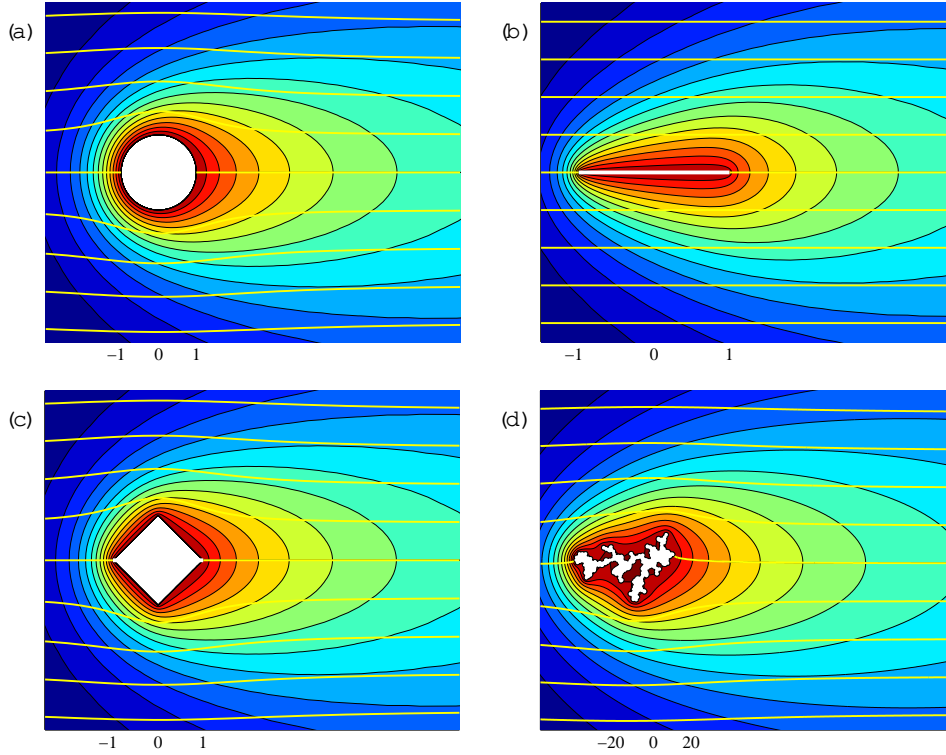


Figure 2. Numerical solutions using the method of Sec. 3 for the concentration profile (color contour plot) and streamlines (open yellow curves) around different absorbing objects in a uniform background potential flow: (a) the unit disk, (b) a finite strip, (c) a square, and (d) an ADLA fractal cluster with $Pe_0 = 1; 2; 1.2$ and 0.05 respectively. The geometries in (b), (c) and (d) are obtained by conformal mapping from (a). Case (b) corresponds to stream line coordinates; case (c) is obtained by the numerical Schwarz-Christoffel mapping (Trefethen 1986); case (d) is obtained from a stochastic, iterated conformal map (Bazant et al., 2003). The renormalized Peclet number is the same, $Pe = 1$, in all cases, which explains why the far-field solutions look the same.

concentration profile, c , satisfies the simplified PDE

$$Pe_0 \frac{\partial c}{\partial t} = \frac{\partial^2 c}{\partial x^2} + \frac{\partial^2 c}{\partial z^2}; \quad (2.1)$$

in "stream line coordinates", $(\xi; \eta)$. The physical significance of this equation is that advection (the left hand side) only occurs along stream lines, while diffusion (the right hand side) also occurs in the transverse direction, along isopotential lines.

Boussinesq's transformation corresponds to a conformal mapping to a plane of a uniform flow, described by a constant velocity U . Therefore, an arbitrary domain, z , as shown in Fig. 1, is mapped to the exterior of a straight line segment, or strip, parallel to the stream lines (which is a branch cut of the inverse map). Some examples are given in Fig. 2. In stream line coordinates, the BCs (1.4) and (1.5) are transformed as follows:

$$c = 1; \quad \frac{\partial c}{\partial \eta} = 0; \quad 2A < \xi < 2A; \quad \text{and} \quad c \rightarrow 0 \text{ as } \xi^2 + \eta^2 \rightarrow 1; \quad (2.2)$$

The constant A is determined so that $4A$ is equal to the difference of the flow potential between two stagnant points, for example, the points S_u and S_d shown in Fig. 1.

2.2. Formulation as an Integral Equation

In stream line coordinates, the advection-diffusion process past a finite strip can be formulated in terms of an integral equation using the classical Green-function method (Stakgold, 1998). For reasons to become clear in Sec. 2.3, we let $x = \xi$, $y = \eta$, $A = 1=2$, and $Pe = Pe_0=2$, so the BVP (2.1)-(2.2) takes the form,

$$2Pe \frac{\partial c}{\partial x} = \frac{\partial^2 c}{\partial x^2} + \frac{\partial^2 c}{\partial y^2} \tag{2.3}$$

$$c = 1; \text{ on } y = 0; \quad -1 < x < 1 \quad \text{and} \quad c = 0; \text{ as } x^2 + y^2 \rightarrow \infty \tag{2.4}$$

The Green function $G(x;y)$ for (2.3), which expresses the concentration profile generated by a unit source flux at the origin, satisfies the PDE,

$$2Pe \frac{\partial G}{\partial x} - \frac{\partial^2 G}{\partial x^2} - \frac{\partial^2 G}{\partial y^2} = -\delta(x)\delta(y) \tag{2.5}$$

After removing the first derivative term by a change of variables and using polar coordinates,

$$G(x;y) = e^{Pe x} F(r; \theta); \tag{2.5}$$

we find that F obeys the Helmholtz equation

$$r^2 F'' + Pe^2 F = -\delta(r)\delta(\theta); \tag{2.6}$$

whose solution is a modified Bessel function of the second kind, $K_0(Pe r)$, where $r = (x^2 + y^2)^{1/2}$. Taking into account the unit normalization, we obtain the Green function,

$$G(x;y) = e^{Pe x} K_0(Pe r) = 2 \dots \tag{2.7}$$

A more systematic derivation of $G(x;y)$ is outlined in Appendix A.

The concentration profile, c , everywhere in stream line coordinates is obtained by convolving the Green function with the flux on the strip,

$$c(x;y) = \int_{-1}^1 G(x - x^0; y) \phi(x^0) dx^0; \tag{2.8}$$

where the factor 2 is included because the flux has the same value,

$$\phi(x) = \frac{\partial c}{\partial y}(x; 0^+) = \frac{\partial c}{\partial y}(x; 0^-);$$

on the upper and the lower sides of the strip, respectively. Therefore, the boundary value problem described by (2.3) and (2.4) is equivalent to finding the $\phi(x)$ that satisfies the integral equation (Pearson, 1957; Wijngaarden, 1966)

$$\int_{-1}^1 e^{Pe(x-x^0)} K_0(Pe|x-x^0|) \phi(x^0) dx^0 = -\phi(x); \quad -1 < x < 1; \tag{2.9}$$

which forms the basis for the theory of solidification in flowing melts (Maksimov, 1976). In this context, it has been analyzed for large and small Pe by Kornev and collaborators, as cited in the introduction. Below, we will extend these results and construct the first analytical approximation that is uniformly accurate in Pe and x .

The reader may worry about the existence and uniqueness of solutions because (2.9) is a Fredholm-type equation of the first kind (with a difference kernel). In the present case, however, the symmetrized kernel, $K_0(Pe|x-x^0|)$, is positive definite, and thus invertible; see Appendix B for an explanation. The integral equation may be approached

using Fourier-type methods because it involves a convolution (Titchmarsh, 1948). We note that the kernel is singular and not of the classical Cauchy type (Muskhelishvili, 1992). It is known that (2.9) admits a solution which can be expanded in terms of Mathieu functions (Rvachev, 1956; Protsenko & Rvachev, 1976), but such representations are impractical for computations over a wide range of Pe , and give no insight into the dependence of the u_x on x and Pe . In this paper, we seek uniformly accurate and physically transparent approximations and thus resort to other methods.

To solve the general BVP (1.3)-(1.5) numerically, one could begin with the integral equation in stream line coordinates (2.9) by expanding the unknown $u_x(x)$, in suitable basis functions, but this representation presents some difficulties. Foremost is the singular behavior of the u_x at the endpoints $x = \pm 1$ as $(x) / 1 = 1 - x^2$; see (2.14) below. Another is the evaluation of the concentration $c(x; y)$ from the $u_x(x)$, which involves additional, costly numerical integration as expressed by (2.8). Below, we avoid these difficulties by applying a more general form of conformal mapping to the original PDE, which enables a very accurate and efficient numerical solution using spectral methods.

2.3. The General Principle of Conformal Invariance

There is a simple way to understand Boussinesq's transformation (Bazant, 2004): The advection-diffusion PDE (1.3) is invariant under conformal changes of variables, even though its solutions are not harmonic functions. As such, the boundary value can be transformed to any convenient geometry by conformal mapping. Stream line coordinates is a good choice for asymptotics, but other choices are better suited for numerical analysis and similarity solutions.

The basic idea is that the Laplacian diffusion operator and the non-Laplacian advection operator transform in the same way under a conformal mapping, $w = f(z)$:

$$\frac{\partial}{\partial z} \frac{\partial c}{\partial z} = J \frac{\partial}{\partial w} \frac{\partial c}{\partial w} \quad \text{and} \quad \frac{\partial}{\partial z} \frac{\partial c}{\partial z} = J \frac{\partial}{\partial w} \frac{\partial c}{\partial w}$$

where $J = \left| \frac{df}{dz} \right|^2$ is the Jacobian factor and subscripts refer to partial derivatives in the two coordinate systems. The same property also holds for conformal mapping to curved surfaces (e.g. stereographic projections), where J is not related to analytic functions. Therefore, all systems of nonlinear equations which are quasilinear and homogeneous in these differential operators are invariant under conformal mapping because the common factor, J , cancels. In addition to our system (1.3), other physical examples in this new class include nonlinear advection-diffusion equations (where the diffusivity, D , depends on the concentration, c , $D = D(c)$) and the Nernst-Planck equations for electrochemical transport (Bazant, 2004).

Here, we exploit this general principle to map the boundary value problem (1.3)-(1.5) to other useful coordinate systems. If $w = \text{Re}(w)$ and $c_w = F(w; \bar{w})$ (where \bar{w} denotes the complex conjugate of w) solve (1.3) in some simple domain, w , then $z = \text{Re}(f(z))$ and $c_z = F(f(z); \bar{f}(z))$ solve (1.3) in an arbitrary mapped domain, $z = g(z)$, where $g(w) = f^{-1}(w)$. The concentration BCs (1.4) are conformally invariant, but, since the BC (1.5) prescribing the background flow is not, due to the gradient, care must be taken in transforming the solution.

For advection-diffusion-limited growth (Bazant et al., 2003), it is natural to let w be the exterior of the unit circle, so our canonical problem is that of a concentrated flow past a circular absorber, shown in Fig. 2 (a), with the velocity potential

$$= \text{Re} \left(w + \frac{1}{w} \right); \quad |w| > 1; \quad (2.10)$$

To reach other geometries, the mapping, $z = g(w)$, must be univalent (conformal and

one-to-one), so it has a Laurent series of the form ,

$$g(w) = A_1 w + A_0 + \frac{A_{-1}}{w} + \dots; \quad |w| > 1;$$

where A_1 is a positive, real constant which defines an effective diameter of z (the "conformal radius"). In order to preserve the BC (1.5) which sets a unit flow speed at $z = 1$, we would need to set the dimensionless flow speed to A_1 at $w = 1$. Instead, we choose to redefine the velocity potential in w to preserve the unit flow speed, as in (2.10), and then define a renormalized Peclet number, $Pe = A_1 Pe_0$, analogous to the time-dependent Peclet number for ADLA defined by Bazant et al. (2003).

The BVP for the concentration w then becomes

$$\text{Per } \nabla^2 c = f c; \quad |w| > 1 \tag{2.11}$$

$$c = 1 \text{ on } |w| = 1; \text{ and } c = 0 \text{ as } |w| \rightarrow \infty \tag{2.12}$$

The physical significance of the renormalized Peclet number is that it determines the far-field solution, independent of the absorber's shape and the bare Peclet number. This point is illustrated in Fig. 2, where the concentration and flow field far away from various objects at $Pe = 1$ looks the same, in spite of extremely different shapes, ranging from a circle to a fractal ADLA cluster. Therefore, we view Pe as the basic parameter in our analysis, from which we define the bare Peclet number, $Pe_0 = Pe/A_1$, for arbitrary domains, in terms of the univalent map from the exterior of the unit circle.

From this perspective, stream line coordinates are obtained by the Joukowski transformation (Carrier et al., 1983), $g(w) = (w + 1/w) = 2$, which maps the unit circular disk onto the finite strip of length 2 centered at the origin along the real axis. The BVP (2.11)-(2.12) is then transformed to the form (2.3)-(2.4) given above. In general, the fluxes on the boundaries ∂_z (the absorber surface) and ∂_w (the unit circle, $w = e^{i\theta}$) are related by

$$w(\theta; Pe) = \int_{\partial_w} g(w; Pe) dz \tag{2.13}$$

where w is the flux on ∂_w and z is the flux on ∂_z . In the case of stream line coordinates (2.3)-(2.4), the flux on the strip, $z(x; Pe)$, is thus related to the flux on the circle, $w(\theta; Pe)$, by

$$w(\theta; Pe) = \int_z \sin \theta z(\cos \theta; Pe) dx \tag{2.14}$$

For a bounded flux on the circle, w , the flux on the strip, z , always diverges as $O((1-x^2)^{-1/2})$ when x approaches 1. Therefore, although we will use the strip geometry, z , for asymptotic analysis in Secs. 4 and 5, the circle geometry, w , is a better starting point for our numerical analysis in Sec. 3. In all cases, however, our goal is to obtain the flux on the circle, the canonical geometry for a finite absorber.

2.4. Similarity Solutions for Semi-Infinite Leading Edges

Before proceeding with our analysis of finite absorbers, we mention a class of similarity solutions for "leading edges" which have relevance for the high-Pe limit of our problem. For this section only, we use the upper half plane, $\text{Im } w > 0$, as our simple domain, w . For a straining velocity field, $(w) = Re w^2, c$, bringing fluid toward the plane, there is a classical similarity solution, $c(w; \bar{w}) = \text{erfc}(\sqrt{Pe_0} \text{Im } w)$, for which the flux on the real axis is a constant, $w = 2 \sqrt{Pe_0}$. (As usual, the complementary error function is defined by $\text{erfc}(z) = \frac{2}{\sqrt{\pi}} \int_z^\infty e^{-t^2} dt$.) If c is interpreted as an out-of-plane velocity component, it corresponds to half of the Burgers' vortex sheet (Burgers, 1948), a famous exact solution to the three-dimensional Navier-Stokes equations. The

same solution also arises in dendritic solidification in a flowing melt, where c is the temperature (Cummings et al., 1999).

Using Burgers' solution, for every conformal map, $w = f(z)$, from the z plane to the upper half plane, there corresponds another similarity solution (Bazant, 2004),

$$c = \text{Re}f(z)^2 \quad \text{and} \quad c = \text{erfc}\left(\frac{r}{\text{Pe}_0} \sqrt{\text{Im}f(z)}\right) \quad \text{for } \text{Im}w = 0: \quad (2.15)$$

Note that the boundary condition $c = 0$ as $|z| \rightarrow \infty$ holds only if $f(z) \sim \frac{1}{z}$ as $|z| \rightarrow \infty$, so these solutions correspond to more general flows near stagnation points. For the purposes of this paper, we discuss two choices for $f(z)$:

(a) $f(z) = \frac{1}{z}$, which maps the entire z plane, with the exception of the branch cut $\text{Im}z = 0; \text{Re}z = x > 0$, onto w . The $(x; y)$ coordinates of the z plane then correspond to the stream line coordinates (Cummings et al., 1999). The flux on the strip is $\dot{m}(x) = \frac{1}{\text{Pe}_0} = x$. This formula can also be derived via replacing the upper limit of integration in (2.9) by 1, and applying the Wiener-Hopf method of factorization (Krein, 1962; Wijngaarden, 1966; Carrier et al., 1983). This procedure is carried out systematically to all orders of approximation in Sec. 4 and by Margetis (2004).

(b) $f(z) = \frac{1}{z+1} = \frac{1}{z} - \frac{1}{1+z}$, which maps the exterior of the circular rim, $|z| > 1$ and $0 < \arg z < 2\pi$, onto w (Bazant, 2004). This solution describes the advection-dominated (high-Pe) fixed point of the ADLA fractal-growth process (Bazant et al., 2003). From (2.15) with $z = re^{i\theta}$ and $r > 1$, we find

$$c(r; \theta) = \text{erfc}\left(\frac{r}{\text{Pe}_0} \sqrt{\frac{1}{r} + \frac{1}{r^2}} \sin \frac{\theta}{2}\right); \quad (\theta) = 2 \frac{r}{\text{Pe}_0} \sin \frac{\theta}{2}; \quad (2.16)$$

which is the leading-order solution for our BVP (2.11)-(2.12) as $\text{Pe}_0 = \text{Pe} \rightarrow \infty$.

The fact that we consider finite absorbers leads to significant analytical and numerical complications, which are the focus of this paper.

3. Numerical Solution

3.1. Conformal Mapping to Polar Coordinates Inside the Unit Disk

In this section we determine the concentration profile c by numerically solving the BVP (2.11)-(2.12). One of the difficulties in applying a numerical method is related to the fact that the region w is unbounded. By invoking conformal invariance again, however, we can apply a transformation that leaves the BVP unchanged yet maps w to a bounded region. In particular, we use inversion, $g(w) = 1/w$, to map the disk exterior onto its interior. Physically, this corresponds to a dipole source of concentrated fluid inside an absorbing circular cylinder, as shown in Fig. 3(a). With $g(w) = re^{i\theta}$ the problem is expressed in the polar coordinates $(r; \theta)$ by

$$r^3 \frac{\partial^2 c}{\partial r^2} + fr^2 + \text{Pe}(1-r^2) \cos \theta \frac{\partial c}{\partial r} + r \frac{\partial^2 c}{\partial \theta^2} + \text{Pe}(1+r^2) \sin \theta \frac{\partial c}{\partial \theta} = 0; \quad (3.1a)$$

$$c = 0; \quad \text{at } r = 0; \quad \text{and} \quad c = 1; \quad \text{at } r = 1; \quad (3.1b)$$

where $r > 1$ and $0 < \theta < 2\pi$. A solution in the $(r; \theta)$ plane is shown in Fig. 3(b).

3.2. Analytical Treatment of Singularities

Before we apply any numerical method to (3.1) directly, we note that the concentration profile c as a function of $(r; \theta)$ exhibits singular behavior as r approaches 0. We first need to modify (3.1a) in order to eliminate this behavior, which undermines the accuracy of

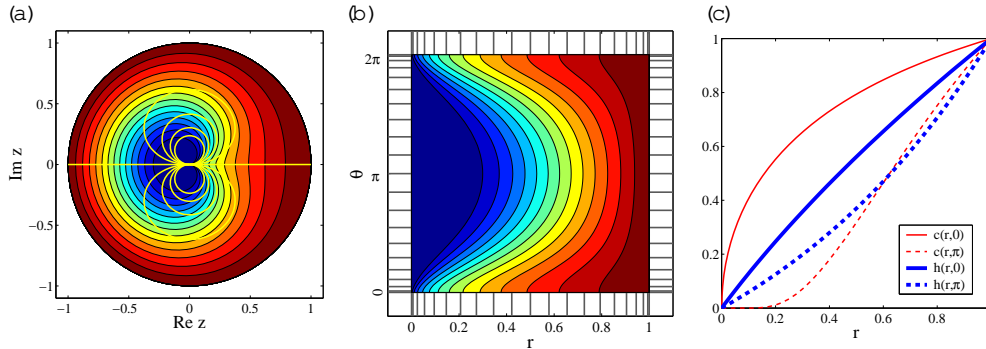


Figure 3. The concentration profile ($Pe = 1$) calculated numerically in the interior of the circular disk is shown (a) in Cartesian coordinates, and (b) in polar coordinates. In (c) the numerically obtained values are shown for $c(r; \theta = 0)$ (thin solid line), $c(r; \theta = \pi)$ (thin dashed line), $h(r; \theta = 0)$ (thick solid line), and $h(r; \theta = \pi)$ (thick dashed line).

our numerical method. From the similarity solution (2.16) and the Green function of Sec. 2.2 we obtain the leading-order behavior

$$c(r; \theta) = O\left(\frac{1}{r}\right) \exp\left(-Pe \frac{1}{r} \left(r \sin^2 \frac{\theta}{2}\right)\right) \quad \text{as } r \rightarrow 0: \quad (3.2)$$

First, the square-root limit $c(r; \theta = 0) = O\left(\frac{1}{r}\right)$ can hardly be dealt with in numerical methods because of the resulting diverging derivative near $r = 0$. Second, the essential singularity at $r = 0$, $c(r; \theta = \pi) = O\left(\frac{1}{r}\right) e^{-Pe/r}$, forces c to change drastically near $r = 0$. Especially when Pe is large, this limiting behavior is extended even to $r < 1 - O(1/Pe)$. To avoid this behavior, we define a function $h(r; \theta)$ by factoring out the leading-order singular behavior of $c(r; \theta)$ as

$$\frac{1}{r} \exp\left(-Pe \frac{1}{r} \left(r \sin^2 \frac{\theta}{2}\right)\right) h(r; \theta) = r c(r; \theta); \quad (3.3)$$

and apply the numerical method shown below directly to this $h(r; \theta)$. Note that the c is multiplied by r in the right-hand side of (3.3) to ensure that $h(r; \theta) = O(r)$ as $r \rightarrow 0$; thus, $h = 0$ at $r = 0$, which is the same condition as for c . Combining (3.1a) and (3.3) we obtain a PDE for $h(r; \theta)$:

$$r^3 \frac{\partial^2 h}{\partial r^2} + Pe(r - r^3) \frac{\partial h}{\partial r} + r \frac{\partial^2 h}{\partial \theta^2} + 2Pe r \sin \frac{\theta}{2} \frac{\partial h}{\partial \theta} + Pe(r \cos \frac{\theta}{2} - 1) + \frac{r^0}{4} h = 0: \quad (3.4)$$

By comparison of (3.1a) and (3.4), we note that the coefficients of the derivatives are simplified in (3.4). Once h is determined from (3.4), c is simply recovered via (3.3), and (3.1b) is obtained as

$$\left(\frac{\partial c}{\partial r}\right)_{(r=1; \theta)} = \left(\frac{\partial h}{\partial r}\right)_{(r=1; \theta)} \frac{1}{2}:$$

Figure 3(c) shows how the singular behavior of c is mitigated by introducing the new variable h .

3.3. Spectral Method

The numerical differentiations with respect to the variables r and θ are carried out by spectral methods (Trefethen, 2000). The spatial nodes, the points $(r_j; \theta_k)$ where the

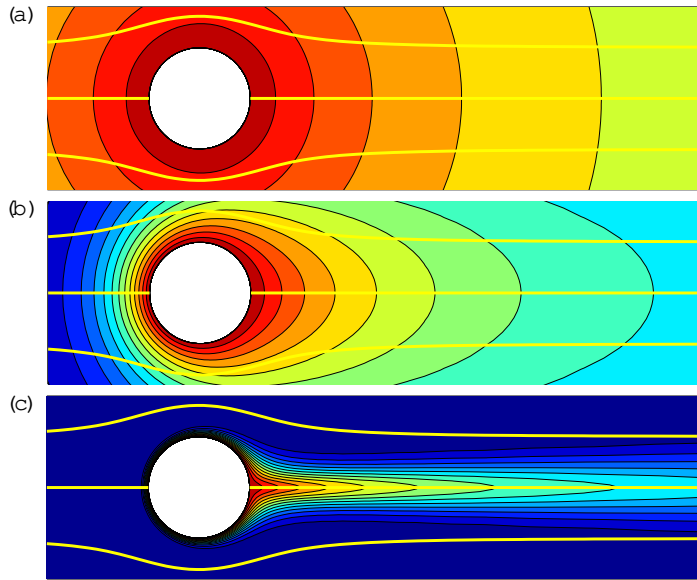


Figure 4. Concentration profile around the unit circular disk for (a) $Pe = 0.01$, (b) $Pe = 1$, and (c) $Pe = 100$.

function is evaluated numerically, are determined by

$$r_j = \frac{1}{2} \left(1 - \cos \frac{j\pi}{N_r} \right) \quad \text{and} \quad \theta_k = \frac{k\pi}{N} ;$$

where $j = 1; \dots; N_r$ and $k = 0; \dots; N$; the nodes have higher density at the endpoints as shown in the frame of Fig. 3 (b). Once the function values are given at the nodes, the derivatives at these points are calculated by interpolation via Chebyshev's polynomials. This procedure is very efficient, as the error in the spectral method is known to decrease exponentially in the number of nodes (Trefethen, 2000). In Figs. 4, 5 we show the concentration $c(r; \theta)$ and the flux $\mathbf{u} \cdot \mathbf{n}$ for Pe of different orders of magnitude using $N_r = 50$ and $N = 100$.

To check the validity of our numerical method, we compare the result for the flux with approximate formulae obtained for high and low Pe . In particular, we use for comparison the asymptotic expansions of Secs. 4 and 5, which are valid for the intermediate range of Peclet numbers $10^3 < Pe < 10^2$. When $N_r = 50$ and $N = 100$ nodes are used for the discretization, the relative error measured as $\frac{\| \mathbf{u}_{num} - \mathbf{u}_{asym} \|}{\| \mathbf{u}_{asym} \|}$ is of the order of 10^{-5} or smaller; here, \mathbf{u}_{num} and \mathbf{u}_{asym} denote the numerical and the asymptotic solutions, respectively and the norm is defined as $\| \mathbf{u} \| = \max_{\theta \in [0; 2\pi]} \int_0^1 |u(r; \theta)| dr$. The reader is referred to Secs. 4 and 5 for details on the asymptotic formulae and the comparisons with the numerical solution. For values of Pe that lie outside the given intermediate range, care should be exercised in using our numerical method, especially when $Pe = 10^4$ or $Pe = 10^3$ as explained below; hence, for such values of Pe we can only resort to the approximate analytical formulae of Secs. 4 and 5.

3.4. Adaptive Mesh for Very High Peclet Numbers

A feature of the solution c that may undermine the accuracy of our numerics is the emergence of boundary layers for sufficiently large Pe . By virtue of (4.16) below we

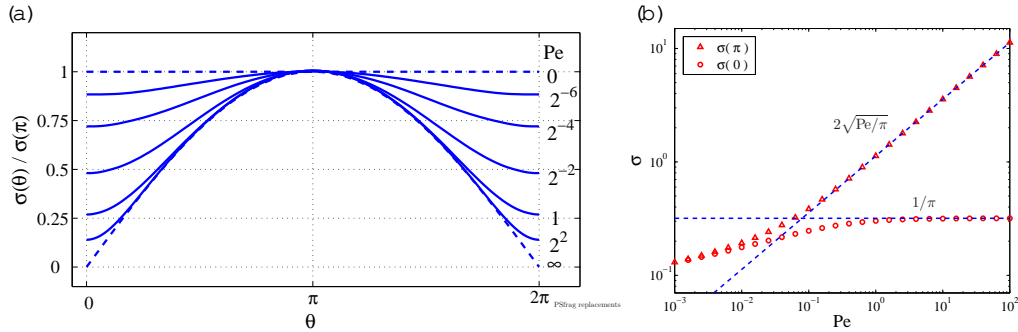


Figure 5. The $u_x(\theta)$ is plotted around the unit disk for different values of Pe : (a) $u_x(\theta) = u_x(\theta)$ for $Pe = 0; 2^{-6}; 2^{-4}; 2^{-2}; 1; 2^2; 1, \infty$, and (b) the values $u_x(\theta = \pi)$ and $u_x(\theta = 0)$ for a range of Pe .

expect that for $Pe \gg 1$,

$$\frac{\partial c}{\partial r} \Big|_{(r=1; \theta)} = \begin{cases} \frac{1}{2} \sqrt{\frac{Pe}{\pi}} \sin(\theta/2) & \text{when } 0 \leq \theta \leq \frac{\pi}{\sqrt{Pe}} \\ 1 & \text{when } \frac{\pi}{\sqrt{Pe}} \leq \theta \leq \pi \end{cases} \quad (3.5)$$

So, $c(r; \theta)$ has boundary layers near $r = 1$ and $\theta = 0; \pi$ whose widths are $O(1/\sqrt{Pe})$, as indicated in Fig. 6 (a). The layer at $\theta = 0$ corresponds to the 'tail' shown in Fig. 4 (c). Thus, the numerical method starts to break down when the node spacing becomes of the order of $1/\sqrt{Pe}$.

We next outline a technique to deal with the case of very high Pe within our numerical procedure. The idea is to introduce a set of independent variables, $\mathbf{x} = \mathbf{x}(r)$ and $\tilde{\theta} = \tilde{\theta}(\theta)$, so that c is a sufficiently smooth function of \mathbf{x} and $\tilde{\theta}$. The following conditions are required for $\mathbf{x}(r)$ and $\tilde{\theta}(\theta)$:

$$\mathbf{x}(0) = 0; \mathbf{x}(1) = 1; \mathbf{x}'(1) = O\left(\frac{1}{\sqrt{Pe}}\right) \quad (3.6)$$

$$\tilde{\theta}(0) = 0; \tilde{\theta}(\pi) = \pi; \tilde{\theta}'(0) = O\left(\frac{1}{\sqrt{Pe}}\right); \quad (3.7)$$

where the prime here denotes differentiation with respect to the argument. Once $\mathbf{x}(r)$ and $\tilde{\theta}(\theta)$ are defined, we find the PDE for $\tilde{h}(\mathbf{x}; \tilde{\theta}) = h(\mathbf{x}(r); \theta)$ from (3.4) by applying the chain rule for the differentiations with respect to r and θ ; for example,

$$\frac{\partial h}{\partial r} = \frac{1}{r^0(\mathbf{x})} \frac{\partial \tilde{h}}{\partial \mathbf{x}}; \quad \frac{\partial^2 h}{\partial r^2} = \frac{1}{r^0(\mathbf{x})^2} \frac{\partial^2 \tilde{h}}{\partial \mathbf{x}^2} - \frac{r^{00}(\mathbf{x})}{r^0(\mathbf{x})^3} \frac{\partial \tilde{h}}{\partial \mathbf{x}}; \quad (3.8)$$

We solve the resulting PDE numerically. A convenient choice for $\mathbf{x}(r)$ and $\tilde{\theta}(\theta)$ is

$$\mathbf{x}(r) = \mathbf{x} + \frac{1}{\sqrt{Pe}} \left(1 - \frac{1}{\sqrt{Pe}} \right) \sin(\mathbf{x}); \quad \tilde{\theta}(\theta) = \tilde{\theta} + \frac{1}{\sqrt{Pe}} \left(1 - \frac{1}{\sqrt{Pe}} \right) \sin \tilde{\theta}; \quad (3.9)$$

The advantage of using \mathbf{x} and $\tilde{\theta}$ instead of r and θ is illustrated in Fig. 6 for $Pe = 100$. The effects of the boundary layers in $(r; \theta)$ are notably suppressed in the formulation using $(\mathbf{x}; \tilde{\theta})$. In Secs. 4 and 5 we discuss the high- and low- Pe asymptotics and their comparisons with the solution determined numerically by the method of this section.

4. Direct Perturbation Analysis For "High" Peclet Numbers

In this section, we derive an approximate analytical solution to the integral equation (2.9) in terms of series expansions produced via suitable iterations in the coordinate

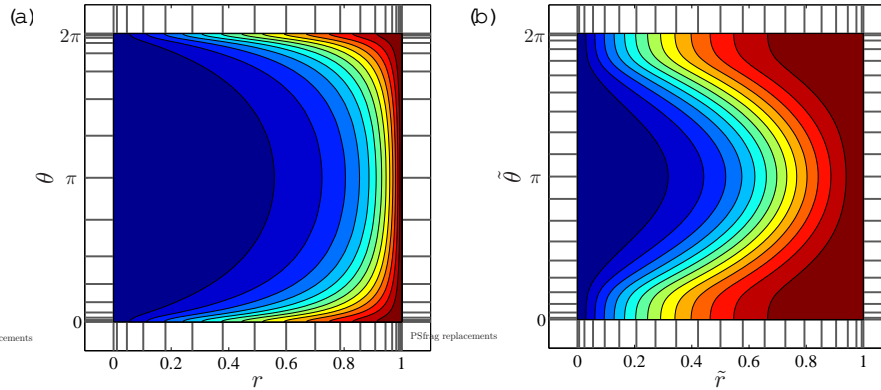


Figure 6. Contour plots of h for $Pe = 100$ (a) in the $(r; \theta)$ plane, and (b) in the $(\tilde{r}; \tilde{\theta})$ plane.

space. We also obtain closed-form expressions for the terms of the iteration series as Pe -dependent multiple integrals. We show that the series is convergent for $Pe = O(1)$, and that retaining only a few of its terms produces accurate results even for $Pe = O(1)$.

4.1. Zeroth-order solution via the Wiener-Hopf method

The starting point of the analysis is the observation that, as discussed in Sec. 2.4, the solution for the semi-infinite strip $-1 < x < +1$ (in the variable notation of (2.9)) provides the leading-order term of the high- Pe asymptotic expansion of the solution for the finite strip up to a distance $O(1/Pe)$ from the endpoint $x = 1$. In order to develop systematically a scheme for the correction terms, we symmetrize the kernel of (2.9) and rescale the independent variable x using $s = Pe(x + 1)$ while we define $\phi_0(s)$ by $\phi_0(x) = (2/Pe)\phi_0(s)$. (The factor $(2/Pe)$ is chosen for later convenience.) The integrodifferential equation (2.9) thus becomes

$$\int_0^{2Pe} ds K_0(\tilde{x}, \tilde{y}) \phi_0(s) = -\frac{2e^{-s}}{Pe}; \quad 0 < s < 2Pe; \quad (4.1)$$

An approximate solution ϕ_0 that is valid to the leading order in Pe is found by taking $Pe \rightarrow \infty$ in the upper limit of integration in (4.1). The resulting integrodifferential equation is

$$\int_0^1 ds K_0(\tilde{x}, \tilde{y}) \phi_0(s) = -\frac{2e^{-s}}{Pe}; \quad 0 < s; \quad (4.2)$$

The solution $\phi_0(s)$ is obtained by the Wiener-Hopf technique (Krein, 1962; Noble, 1988). Here we outline the basic steps of this method, which are also applied to other, similar integral equations below. First, we extend the validity of (4.2) to $-1 < s < 1$ via modifying its right hand side,

$$\int_{-1}^1 ds K_0(\tilde{x}, \tilde{y}) \phi_0(s) = -\frac{2}{Pe} f e^{-s} u(s) + p(s)g; \quad -1 < s < 1; \quad (4.3)$$

where $\phi_0(s)$ is taken to be zero for $s < 0$, $u(s)$ is the Heaviside function ($u(s) = 0$ for $s < 0$ and $u(s) = 1$ for $s > 0$), and $p(s)$ is an unknown function which has non-zero values only for $s < 0$. Next, we apply the Fourier transform in s to (4.3). Defining the Fourier transform, $\tilde{\phi}_0(k)$, of $\phi_0(s)$ as

$$\tilde{\phi}_0(k) = \int_{-1}^1 ds \phi_0(s) e^{iks} \quad \text{where} \quad \phi_0(s) = \int_{-1}^1 \frac{dk}{2} e^{-iks} \tilde{\phi}_0(k); \quad (4.4)$$

(4.3) yields

$$\frac{\tilde{\phi}_0(k)}{1+k^2} = \frac{1}{2} \frac{1}{1+ik} + \phi(k) \quad (4.5)$$

By simple algebraic manipulations the last equation becomes

$$\frac{\tilde{\phi}_0(k)}{1+ik} \frac{1}{1+ik} = \frac{1}{2} \frac{1}{1+ik} + \phi(k); \quad (4.6)$$

where the left hand side defines a function analytic in the lower half k plane, $\text{Im } k < 0$ for a small positive ϵ , and the right hand side defines a function analytic in the upper half k plane, $\text{Im } k > \epsilon$; each of these functions vanishes as $|k| \rightarrow \infty$ in the corresponding half plane. Thus, the two sides of (4.6) together define an entire function of k , which is identically zero by Liouville's theorem (Carrier et al., 1983). It follows that in the region of overlap, $\epsilon < \text{Im } k < \epsilon$, the solution is $\tilde{\phi}_0(k) = (1+ik)^{-1/2}$. Inversion of this formula yields

$$\phi_0(s) = \frac{1}{s} e^{-s}; \quad 0 < s < 1 \quad (4.7)$$

4.2. Leading-order Uniformly Accurate Approximation

The deviation of $\phi_0(s)$ in (4.7) from the actual solution $\phi(s)$ of the finite strip is due to the effect of a fictitious, "misplaced" flux source lying in $2Pe < s$, which is present in (4.2). Therefore a correction term must be found for $\phi_0(s)$ by considering a "correction source" placed on the original strip, $0 < s < 2Pe$, to compensate for the effect of the misplaced source. Marquetis (2004) further develops this approach and places it on a firm mathematical ground using Fourier transforms and a generalization of the Wiener-Hopf method. We proceed to calculate the correction to ϕ_0 iteratively. Accordingly, the solution $\phi(s)$ is sought in terms of the series

$$\phi(s) = \phi_0(s) + \phi_1(s) + \phi_2(s) + \phi_3(s) + \dots + \phi_n(s) + \dots; \quad (4.8)$$

where each term $\phi_n(s)$ corresponds to suitable source corrections as described below.

We consider a half-line as the domain of the correction $\phi_1(s)$, as we did to obtain ϕ_0 , but in the region $1 < s < 2Pe$ instead of the region $0 < s < 1$. The term ϕ_1 is determined so that its effect compensates for the integrated effect of $\phi_0(s)$ in the region $2Pe < s$. Hence, the correction $\phi_1(s)$ satisfies

$$\int_1^{2Pe} ds^0 K_0(j\beta - s^0) \phi_1(s^0) = \int_{2Pe}^{\infty} ds^0 K_0(j\beta - s^0) \phi_0(s^0); \quad s < 2Pe; \quad (4.9)$$

where the right-hand side is known. The next-order corrections can be formulated and interpreted in a similar way; the correction ϕ_n compensates for the effect of the misplaced source corresponding to ϕ_{n-1} , where ϕ_{n-1} and ϕ_n are defined in half-lines that together cover the entire real axis and overlap only in the region of the finite strip. In general, ϕ_{n-1} satisfy the recursion relations

$$\int_1^{2Pe} ds^0 K_0(j\beta - s^0) \phi_{n-1}(s^0) = \int_{2Pe}^{\infty} ds^0 K_0(j\beta - s^0) \phi_{n-2}(s^0); \quad (4.10a)$$

$$\int_0^{2Pe} ds^0 K_0(j\beta - s^0) \phi_n(s^0) = \int_1^{2Pe} ds^0 K_0(j\beta - s^0) \phi_{n-1}(s^0); \quad (4.10b)$$

where we made the change of variable from s to $v = 2Pe - s$ so that the integral equation for $\phi_{n=2k+1}$ has the same form as the one for $\phi_{n=2k}$. The variables s and v are both

positive ($s > 0$ and $v > 0$), the left endpoint ($x = -1$) of the strip corresponds to $s = 0$ and the right endpoint ($x = 1$) corresponds to $v = 0$.

The various u_n can be obtained successively, order by order, by applying the Wiener-Hopf method (Krein, 1962; Noble, 1988) directly to (4.10), but the procedure becomes increasingly cumbersome with n . Instead, we propose a systematic procedure that facilitates the derivation of a closed-form expression for each u_n . For this purpose, we introduce an operator, L , that relates u_{n-1} and u_n by $L[u_{n-1}] = u_n$. By (4.10) L is linear. In order to obtain u_1 , we notice that the leading-order solution $u_0(s)$ can be represented as an integral over a variable, t_0 ,

$$u_0 = \frac{r}{s} e^{-s} = \int_0^{\infty} dt_0 e^{-s(1+t_0^2)}; \quad (4.11)$$

Then L acts on u_0 to yield u_1 as

$$u_1 = \int_0^{\infty} dt_0 L[e^{-s(1+t_0^2)}]; \quad (4.12)$$

where the order of L and integration is safely interchanged. The advantage of using the t_0 -representation is that $e^{-s(1+t_0^2)}$, as a function of s , has a Fourier transform simpler than the Fourier transform of $u_0(s)$ itself. The function $L[e^{-s(1+t_0^2)}]$ is found by the Wiener-Hopf method (Krein, 1962) as described in Sec. 4.1, and u_1 follows by (4.12):

$$L[e^{-s(1+t_0^2)}] = e^{-2Pe(1+t_0^2)} \frac{e^{-v}}{v(2+t_0^2)} \operatorname{erfc} \frac{v}{v(2+t_0^2)}; \quad (4.13)$$

$$u_1(v) = K_0(2Pe) \frac{e^{-v}}{v} \int_0^{\infty} dt_0 e^{-(2Pe-v)(1+t_0^2)} \operatorname{erfc} \frac{v}{v(2+t_0^2)}; \quad (4.14)$$

Because u_0 and u_1 are accurate arbitrarily close to the left edge ($s = 0$) and the right edge ($v = 0$) of the strip, respectively, $u_0 + u_1$ yields a leading-order approximation for u as $Pe \rightarrow \infty$ valid over the entire finite strip. The corresponding approximation for the $u(x) = \frac{r}{2} Pe^{-s(x)}$ is $u_1 + u_2$, which is given by

$$(x) \quad u^{(h)}(x) = \frac{r}{2} \left(\frac{Pe}{2(1+x)} + \frac{K_0(2Pe)e^{2Pex}}{2(1-x)} \right) \int_0^{\infty} \frac{e^{-(1+x)t_0^2}}{2} \operatorname{erfc} \frac{v}{(2Pe+t_0^2)(1-x)} dt_0 \quad (4.15)$$

for the geometry of the finite strip, and

$$(j) \quad u^{(h)}(j) = \frac{r}{2} \left(\frac{Pe}{2} j \sin \frac{j}{2} + \frac{1}{2} K_0(2Pe) e^{2Pe \cos \frac{j}{2}} j \cos \frac{j}{2} \right) \int_0^{\infty} \frac{j \sin \frac{j}{2}}{2} \frac{e^{-(1+\cos \frac{j}{2})t_0^2}}{2} \operatorname{erfc} \frac{v}{(2Pe+t_0^2)(1-\cos \frac{j}{2})} dt_0 \quad (4.16)$$

for the geometry of the unit circular disk. In the last formula we changed the variable to $v = Pe t_0$. Equation (4.15) has been obtained by Komev & Chugunov (1988) and Alimov et al. (1998) in the physical context of artificial freezing; these authors did not use the operator L in their method and apparently did not obtain higher-order terms. An elaborate mathematical procedure for asymptotic solutions to the rel-

^y In the remaining integrals of this section the range of integration is understood to be from -1 to 1 unless it is stated otherwise.

evant class of integral equations on the basis of kernel approximations is described in (Aleksandrov & Belokon, 1968) and (Aleksandrov & Pozharskii, 1999). We note that $\phi_0(x)$ and $\phi_1(x)$ are singular at $x = -1$ and $x = 1$, respectively, the edges of the finite strip; these singularities are properly removed after the strip is mapped onto the unit disk.

4.3. Exact Higher-Order Terms

In an effort to obtain further insight into the nature of the solution of (2.9), we next derive exact, closed-form expressions for ϕ_n for all n in terms of iterated, multiple integrals. For this purpose, we exploit the L operator introduced above. We observe that (4.13) has the integral representation

$$L[\phi^{s(1+t_0^2)}] = \int_{t_1}^Z \frac{e^{2Pe(1+t_0^2)}}{2+t_0^2} \frac{t_1^2}{(2+t_0^2+t_1^2)} e^{v(1+t_1^2)}; \quad (4.17)$$

where the last factor in the integrand has the same form as the $e^{s(1+t_0^2)}$ term, on which the L acts in (4.12), with the s being replaced by v and the t_0 being replaced by t_1 . It follows that the ϕ_n is expressed as the n -th power of L acting on a term of the form $e^{s(1+t^2)}$, $L^n[\phi^{s(1+t^2)}]$. Thus, by induction, ϕ_n is expressed as an iterated, multiple integral of the independent variables s or v ,

$$\phi_n(u) = e^{2nPe} \int_{t_0}^Z \int_{t_1}^Z \int_{t_2}^Z \dots \int_{t_n}^Z (Q_{n-1}R_n) e^{u(1+t_n^2)}; \quad (4.18)$$

where $u = s$ for even n and $u = v$ for odd n , and Q_n and R_n are defined by

$$Q_n = \frac{e^{2Pe t_n^2}}{2+t_n^2}; \quad R_n = \frac{t_n^2}{(2+t_{n-1}^2+t_n^2)}; \quad (4.19)$$

We next single out the singular behavior of ϕ_n at $u = s = 0$ (left edge) or $u = v = 0$ (right edge), before we obtain the (physical) u_x on the boundary. For this purpose, the integral over t_n in (4.18) is expressed in terms of the integration variable $\xi = \frac{t_n}{u}$ as

$$\int_{t_n}^Z Q_{n-1}R_n e^{u(1+t_n^2)} = \frac{e^{2Pe}}{u} \int_{\xi}^Z \frac{Q_{n-1} \xi^2 e^{-\xi^2}}{f u (2 + \xi_{n-1}^2) + 2g}; \quad (4.20)$$

thus, ϕ_n has the singularity $u^{-1/2}$ as $u \rightarrow 0$ for all n , where the prefactor is now evident in compact form. From (4.18) and (4.20) $\phi_n(x)$ is given by

$$\phi_{n=2k}(x) = \frac{e^{2kPe}}{1+x} \int_{t_0}^Z \int_{t_1}^Z \int_{t_2}^Z \dots \int_{t_n}^Z (Q_{n-1}R_n) e^{u(1+t_n^2)}; \quad (4.21a)$$

$$\phi_{n=2k+1}(x) = \frac{e^{2(n-x)Pe}}{1-x} \int_{t_0}^Z \int_{t_1}^Z \int_{t_2}^Z \dots \int_{t_n}^Z (Q_{n-1}R_n) e^{u(1+t_n^2)}; \quad (4.21b)$$

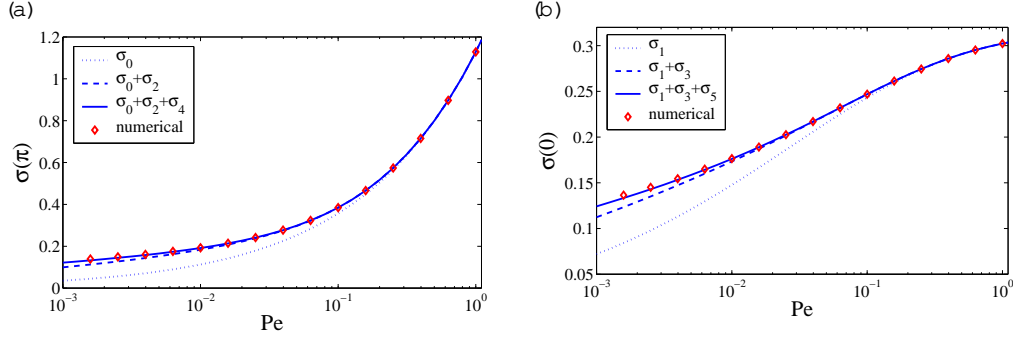


Figure 7. Asymptotic approximations for high Pe compared with our numerical solution: (a) Upstream u_x , ($\xi = \pi/2; Pe$) and (b) downstream u_x , ($\xi = 0; Pe$). The integrals in the asymptotic corrections, $n = 1 \dots 5$, were performed numerically.

On the unit circle $\sigma_n(\xi)$ is free of singularities in ξ and is expressed as

$$\sigma_{n=2k}(\xi) = \frac{2^k}{Pe} e^{2nPe} \int_0^{2\pi} \prod_{j=1}^n \left(\frac{Z}{Z - e^{j\xi}} \right) dt_0 \dots dt_{n-1} (Q_0 R_1) \dots dt_{n-1} (Q_{n-1} R_n) \quad (4.22a)$$

$$\sigma_{n=2k+1}(\xi) = \frac{2^k}{Pe} e^{2(n \cos \xi)Pe} \int_0^{2\pi} \prod_{j=1}^n \left(\frac{Z}{Z - e^{j\xi}} \right) dt_0 \dots dt_{n-1} (Q_0 R_1) \dots dt_{n-1} (Q_{n-1} R_n) \quad (4.22b)$$

It has not been possible to evaluate σ_n from (4.22) in simple closed form, except for $n = 1; 2$ as described by (4.16). However, the numerical integrations over the variables t_j ($j = 1; 2; \dots; n$) for each n can be carried out efficiently by using recursion.

We verify numerically that the sum, $\sigma_0 + \sigma_1 + \dots + \sigma_n$, calculated for finite n via the numerical integration of (4.22), indeed approaches the numerical solution of Sec. 3. In Fig 7, we show a comparison of the numerical solution of Sec. 3 for $\sigma(0)$ and $\sigma(\pi/2)$ with formula (4.22) for different values of n . Because $\sigma_{n=2k}(\xi)$ and $\sigma_{n=2k+1}(\xi)$ vanish at $\xi = 0$ and $\xi = \pi$, respectively, the term $\sigma_{n=2k}(\xi)$ affects only $\sigma(\pi/2)$ whereas the term $\sigma_{n=2k+1}(\xi)$ affects only $\sigma(0)$.

Remarkably, with only a few terms, the approximation is uniformly accurate down to values of Pe of order 10^{-3} , which could hardly be called "high". This suggests that there may be an intermediate region of overlap between asymptotic approximations for high and low Pe . Indeed, by combining such approximations below, we will construct a very accurate approximation for all ξ and all Pe .

4.4. Convergence of the Asymptotic Series

We next discuss the convergence properties of the asymptotic series $\sum_{n=0}^{\infty} \sigma_n(\xi)$ for ξ on the unit circle. Because the maximum of $\sigma_n(\xi)$ occurs at $\xi = \pi$ for $n = 2k$ and at $\xi = 0$ for $n = 2k + 1$, it is readily shown that

$$\frac{\sigma_{n=2k}}{\sigma_{n=2k-1}} \sim \frac{2^k}{Pe} \quad \text{and} \quad \frac{\sigma_{n=2k}}{\sigma_{n=2k+1}} \sim e^{4Pe k} F_{2k} \quad (4.23)$$

where F_n is given by

$$F_0 = 1; \quad F_{n-1} = \frac{1}{2} \int_{t_0}^Z \int_{Q_0 R_1}^Z \int_{dt_{n-1}}^Z (Q_{n-2} R_{n-1}) Q_{n-1}; \quad (4.24)$$

and Q_k and R_k are defined in (4.19). In particular, for $n = 1, 2$, F_n are evaluated in simpler forms:

$$F_1 = \frac{e^{2Pe}}{2} K_0(2Pe); \quad F_2 = \frac{e^{4Pe}}{2} \frac{K_0(2Pe)^2}{2} \int_{2Pe}^Z dt K_0(t)^2; \quad (4.25)$$

We have not been able to further simplify the expressions for $F_{n>2}$. We now show that each F_n is bounded by a function of Pe that ensures convergence of the series $\sum_{n=0}^{\infty} F_n$ for $Pe > 0(1)$. By noting that $Q_n < 2^{1-2n} e^{2Pe t_n^2}$ and $R_n < 1$, we find

$$F_n < 2^{n-2} (4Pe)^{n-2}; \quad (4.26)$$

for any $Pe > 0$. Hence, by (4.23) the series $\sum_{n=0}^{\infty} F_n$ is characterized by geometric convergence in the parameter $Pe^{1/2}$ for $Pe > 0(1)$. Finally, for large Pe and fixed n the asymptotic behavior of F_n with respect to Pe is obtained via scaling the original variables t_k as $t_k = t_k / 2Pe$ ($k = 0, \dots, n-1$),

$$F_{n-1} \sim \frac{1}{2} \frac{1}{Pe} \frac{1}{16} \frac{1}{Pe^{3/2}} \dots^{n-1} \text{ as } Pe \rightarrow \infty; \quad (4.27)$$

Formulae (4.26) and (4.27) indicate that the series $\sum_{n=0}^{\infty} F_n$ converges geometrically for a wide range of Pe .

We check numerically that F_n decays exponentially in n for a wide range of Pe , $F_n \sim \lambda^n$ as $n \rightarrow \infty$ where $\lambda = \lambda(Pe) > 0$ is the "decay rate" of F_n , which is independent of n . For this purpose, we examine the ratio $F_n = F_{n+1}$ as a function of both n and Pe , expecting that this ratio approaches a constant for fixed Pe as n becomes sufficiently large, as shown in Figs. 8(a), (b), (c). From Fig. 8(d) we find that the relative error in the approximation of F_n by the sum $\sum_{k=1}^5 F_k$ becomes higher than 1% only when $Pe < 6.5 \times 10^3$.

5. Uniformly Accurate Asymptotics For Low Peclet Numbers

In this section we solve approximately the integral equation (2.9) for the surface $u(x)$, for all x in $(-1; 1)$, when Pe is sufficiently small, $Pe < 0(1)$. For this purpose, we define the dependent variable $v(x) = e^{Pe x} u(x)$. Equation (2.9) thus becomes

$$\int_{-1}^Z dx K_0(Pe x - x^0) v(x^0) = e^{Pe x}; \quad -1 < x < 1; \quad (5.1)$$

Because the argument of the kernel is also sufficiently small, $Pe x - x^0 < 0(1)$, we invoke the expansion

$$K_0(Pe x - x^0) \sim \int_0^{\infty} (Pe x - x^0)^m \ln \frac{Pe x - x^0}{2} + \sum_{m=0}^{\infty} \frac{(m+1)}{(m!)^2} \frac{(Pe x - x^0)^{2m}}{2}; \quad (5.2)$$

where it is understood that

$$I_0(Pe x - x^0) \sim \sum_{m=0}^{\infty} \frac{2^{-2m} Pe^{2m} (x - x^0)^{2m}}{(m!)^2}; \quad (5.3)$$

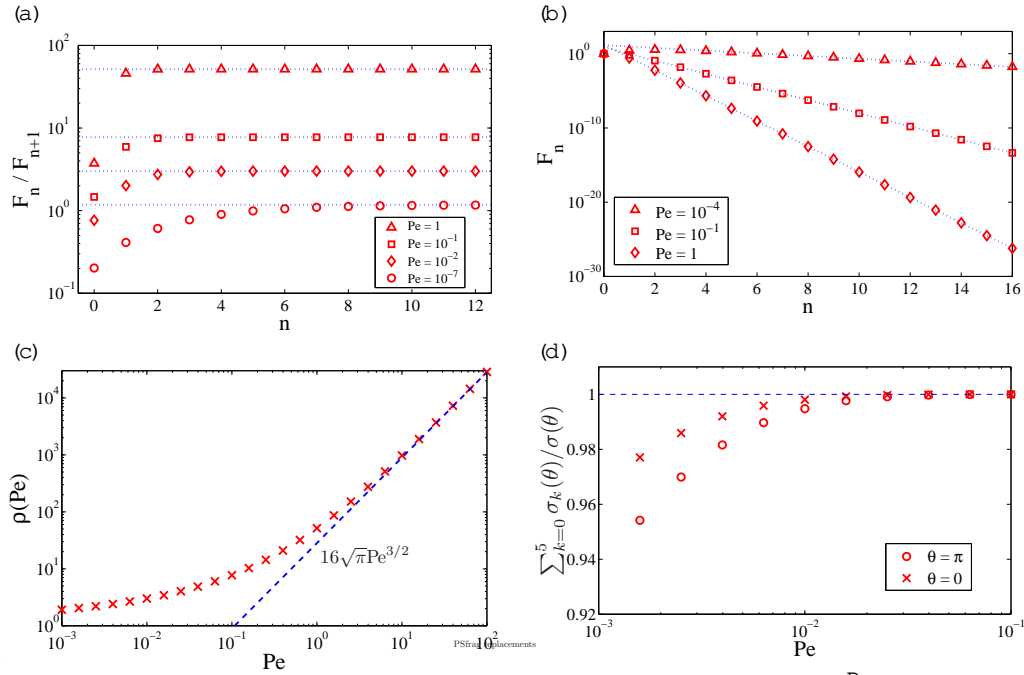


Figure 8. Numerical evidence for the convergence of the iteration series $\rho_n = F_n/F_{n+1}$. (a) The ratio F_n/F_{n+1} as a function of n for different values of Pe . The convergence of ρ_n is guaranteed if $F_n/F_{n+1} > 1$ by virtue of (4.23). (b) The term F_n as a function of n for different values of Pe . (c) The decay rate $\rho(Pe)$ of F_n as a function of Pe , where $\rho(Pe) = \lim_{n \rightarrow \infty} F_n/F_{n+1}$. The asymptotic behavior (4.27) is shown to be attained for $Pe > 10$. (d) The ratio of $\sum_{k=0}^5 \sigma_k(\theta)/\sigma(\theta)$ to $\sigma(\theta)$ as a function of Pe and $\theta = 0$; $\sigma(\theta)$ is evaluated numerically by the method of Sec. 3.

and $\psi(z)$ is the logarithmic derivative of the Gamma function, $\psi(z) = \frac{d}{dz} \ln \Gamma(z)$. It was first pointed out by Pearson (1957) that the resulting integral equation can be solved exactly for any finite number of terms, M , but the procedure becomes increasingly cumbersome with M .

To leading order we consider $M = 0$ in (5.2) and (5.3). Equation (5.1) thus reduces to a variant of Carleman's equation (Carleman, 1922),

$$\int_1^{\infty} dx^0 \ln(x^0/x^1) f_0(x^0) = C_1 e^{Pe x^0}; \quad (5.4)$$

where $\gamma = 0.577215$ is the Euler number and $f_0(x)$ is the corresponding approximation for $f(x)$, and C_1 is the constant

$$C_1 = \left[\gamma + \ln(Pe=2) \right] \int_1^{\infty} dx^0 f_0(x^0); \quad (5.5)$$

Introducing the function

$$\psi(z) = \frac{Pe}{2} \frac{\int_1^{\infty} dx^0 f_0(x^0)}{z}; \quad (5.6)$$

and defining two limit values

$$\psi(x) = \lim_{x \rightarrow 0} \psi(x) = \frac{Pe}{2} \lim_{x \rightarrow 0} \int_1^{\infty} dz^0 \frac{f_0(z^0)}{z^0 x}; \quad (5.7)$$

the integral equation (5.4) is equivalent to the following system of equations:

$$\begin{aligned} \psi(x) &= \frac{1}{2\pi} \int_{-1}^1 dx^0 \ln|x-x^0| \psi_0(x^0) \\ &= \frac{1}{2\pi} \int_{-1}^1 dx^0 [C_1 e^{Pe x^0}] = \frac{1}{Pe} \frac{1}{2\pi} \int_{-1}^1 e^{Pe x^0} dx^0; \end{aligned} \quad (5.8)$$

$$\psi(x) + \psi'(x) = \frac{1}{2\pi} \int_{-1}^1 dx^0 \operatorname{Res} \frac{\psi_0(z^0)}{z^0 - x}; z^0 = x = \frac{1}{2\pi} \int_{-1}^1 dx^0 \psi_0(x^0); \quad (5.9)$$

First, we find $\psi(z)$ via applying directly the Mittag-Leffler expansion theorem to (5.8) following Carrier et al. (1983):

$$\psi(z) = \frac{1}{2\pi i} \int_{-1}^1 dx^0 \frac{1}{x^0 - z} e^{Pe x^0} + A; \quad (5.10)$$

where $(2\pi i)^{-1} A$ is the limit as $z \rightarrow 1$ of the function $\psi(z)$; by inspection of (5.6),

$$A = \frac{1}{2\pi} \int_{-1}^1 dx^0 \psi_0(x^0); \quad (5.11)$$

We recognize that the constant C_1 of (5.5) is $C_1 = [1 + \ln(Pe=2)]A$.

Next, we obtain the approximate solution $\psi_0(x)$ in terms of this A by (5.8):

$$\psi_0(x) = \frac{1}{2\pi} \int_{-1}^1 dx^0 \frac{1}{x^0 - x} e^{Pe x^0} + A; \quad (5.12)$$

where $(P)^{-1}$ denotes the principal value of the integral. In order to determine the unknown constant A , we multiply both sides of (5.4) by $(1-x^2)^{-1/2}$ and integrate over $(-1; 1)$ by use of the elementary integral Carrier et al., 1983)

$$\int_{-1}^1 dx \frac{\ln|x-x^0|}{1-x^2} = \ln 2; \quad (5.13)$$

A few comments on this result are in order. It can be obtained via differentiating the left hand side with respect to x^0 , and thus converting the integral to a Cauchy principal value which is found directly to vanish identically. Hence, the original integral is independent of x^0 and can be evaluated for $x^0 = 0$ by changing the variable to $x = (1-i\epsilon)/(2i)$, where ϵ moves on the unit circle, and applying the residue theorem Carrier et al., 1983). We thus find

$$A = \frac{1}{1 + \ln(Pe=4)} \int_{-1}^1 dx \frac{e^{Pe x}}{1-x^2}; \quad (5.14)$$

$$\psi_0(x) = \frac{1}{2\pi} \int_{-1}^1 dx^0 \frac{1}{x^0 - x} e^{Pe x^0} + \frac{1}{1 + \ln(Pe=4)} \int_{-1}^1 dx^0 \frac{e^{Pe x^0}}{1-x^2}; \quad (5.15)$$

It is straightforward to carry out the integrations in (5.15). The second integral on the right-hand side is simply a modified Bessel function of the first kind:

$$\int_{-1}^1 dx \frac{e^{Pe x}}{1-x^2} = \int_0^1 dt e^{Pe \cos t} = J_0(iPe) = I_0(Pe); \quad (5.16)$$

The remaining integral can be converted to one that is directly amenable to numerical

computation for $Pe \gg 1$. By defining

$$I(Pe; x) = (Pe)^{-1} \int_0^1 dx \frac{1}{1-x^2} e^{Pe(x-x^2)}; \quad (5.17)$$

we evaluate the derivative

$$e^{Pe x} \frac{\partial I}{\partial Pe} = \int_0^1 dx \frac{1}{1-x^2} e^{Pe x} = [I_0(Pe) - I_0^*(Pe)] = \frac{I_1(Pe)}{Pe}; \quad (5.18)$$

where I_1 is the modified Bessel function of the first kind. An expression for the integral (5.17) then follows by direct integration in Pe of (5.18):

$$I(Pe; x) = I(0; x) + \int_0^{Pe} dt e^{tx} \frac{I_1(t)}{t}; \quad (5.19)$$

where

$$I(0; x) = (1-x^2) \frac{d}{dx} \int_0^1 dx \frac{\ln(x-x^2)}{1-x^2} \quad x = x; \quad (5.20)$$

Hence,

$$I(Pe; x) = x \int_0^{Pe} dt e^{tx} \frac{I_1(t)}{t}; \quad (5.21)$$

The approximation

$$+ \ln(Pe=4) \quad K_0(Pe=2) \quad (5.22)$$

and the use of (5.16), (5.21) and $(x) = e^{Pe x}$, (x) furnish a low- Pe approximation for the flux on the boundary of the finite strip, $(^{(b)}) = e^{Pe x}$, (x) ,

$$(x) \quad (^{(b)}) (x) = \frac{1}{1-x^2} \frac{I_0(Pe)}{K_0(Pe=2)} e^{Pe x} + \int_0^{Pe} dt e^{tx} \frac{I_1(t)}{t}; \quad (5.23)$$

Hence, by virtue of (2.14), the flux on the unit circle is

$$() \quad (^{(b)}) () = \frac{I_0(Pe)}{K_0(Pe=2)} e^{Pe \cos} + \int_0^{Pe} dt e^{t \cos} \frac{I_1(t)}{t}; \quad (5.24)$$

We note in passing that the integral in (5.23) can be expressed as a powers series in Pe . With the series expansions

$$e^{tx} = \sum_{n=0}^{\infty} \frac{t^n x^n}{n!}; \quad \frac{I_1(t)}{t} = \sum_{m=0}^{\infty} \frac{t^{2m}}{2^{2m+1} m!(m+1)!}; \quad (5.25)$$

it is straightforward to derive the expansion

$$\int_0^{Pe} dt e^{xt} \frac{I_1(t)}{t} = \sum_{l=0}^{\infty} \frac{Pe^{2l+1} X^l}{2^{2l+1} (2m)!(l-m)!(l+m+1)!} x^{2m} + \sum_{l=0}^{\infty} \frac{Pe^{2(l+1)} X^l}{2^{2(l+1)} (2m+1)!(l-m)!(l+m+1)!} x^{2m+1}; \quad (5.26)$$

A few comments on formula (5.23) are in order. Aleksandrov & Belkon (1967) expanded to high orders the kernels of the relevant class of singular integral equations and derived in generality a more accurate yet complicated formula for the solution. The procedure here, though being based on simply taking $M = 0$ in (5.2) and (5.3), leaves

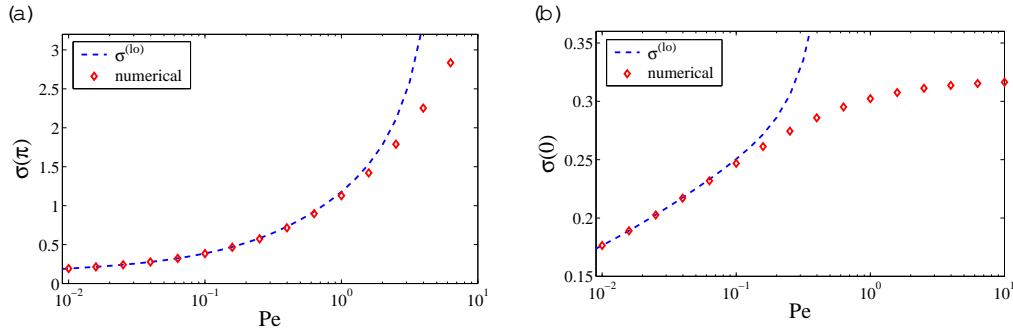


Figure 9. The asymptotic approximation $\sigma^{(lo)}(\pi; Pe)$ in (5.24) compared to the numerical solution of Sec. 3 for a range of low Pe. (a) Upstream $u_x, \sigma(\pi)$ ($\theta = \pi; Pe$), and (b) downstream $u_x, \sigma(0)$ ($\theta = 0; Pe$).

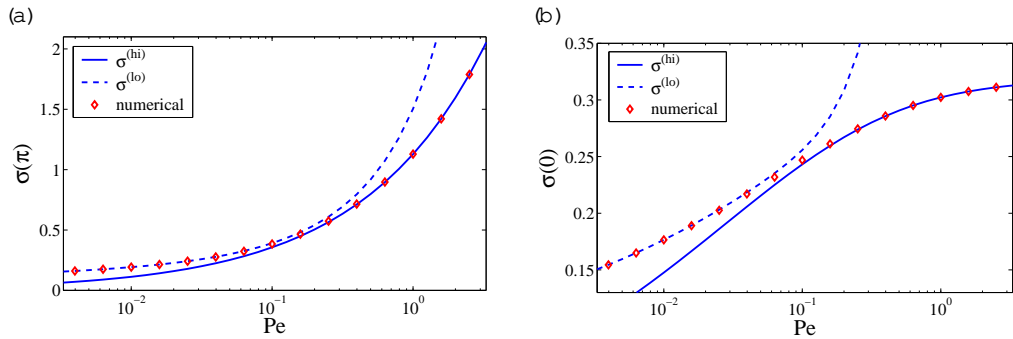


Figure 10. Plots of formulae (4.16) for $\sigma^{(hi)}$ and (5.24) for $\sigma^{(lo)}$ versus Pe in the same graph as the plot for the solution evaluated numerically by the method of Sec. 3. (a) Upstream $u_x, \sigma(\pi)$ ($\theta = \pi; Pe$). (b) Downstream $u_x, \sigma(0)$ ($\theta = 0; Pe$).

intact the right-hand side of (5.1) and applies (5.22); our approximate formula for $\sigma(x)$ turns out to be accurate for an extended range of low Pe. Figure 9 shows a comparison of (5.24) with the numerical solution of Sec. 3 for a range of low Peclet numbers.

6. Uniformly Accurate Formula for All Positions and Peclet Numbers

6.1. Connecting the High and Low Pe Approximations for the u_x

In Secs. 4 and 5 we derived asymptotic formulae for the surface u_x on the boundary of the unit circular disk (or finite strip) that are valid for sufficiently high or sufficiently low Pe; these expressions, $\sigma^{(hi)}$ and $\sigma^{(lo)}$ in (4.16) and (5.24), respectively, hold for all values of the local coordinate of the absorber boundary, although we did not analyze to what extent the approximations are uniformly valid. Comparisons with the numerical results in Figs. 7 and 9 show that the approximations are comparably accurate for the rear stagnation point ($\theta = 0$) and forward stagnation point ($\theta = \pi$). We have also checked that, for fixed Pe, the errors are also comparable at intermediate values of the local coordinate ($0 < \theta < \pi$). In Fig. 10, we show that the two approximations, $\sigma^{(hi)}$ and $\sigma^{(lo)}$, nearly overlap for some range of values Pe near the value $Pe = 0.1$, while remaining remarkably close to the "exact" numerical solution from Sec. 3.

The existence of a regime of overlapping accuracy allows us to construct an analytical formula for σ , accurate for all values of Pe and the local coordinate of the absorbing

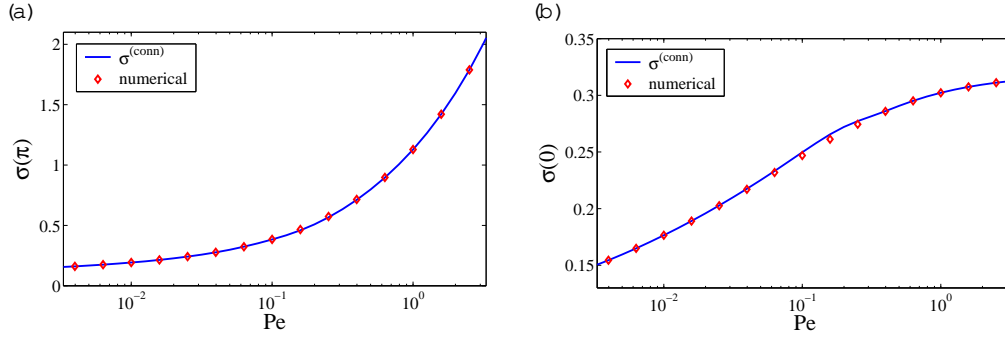


Figure 11. P plots of the connection formula, $\sigma^{(\text{conn})}$, from Eqs. (6.1) and (6.3), in comparison to the numerical solution of Sec. 3: (a) Upstream ux, $\sigma^{(\text{conn})}(\pi)$, and (b) downstream ux, $\sigma^{(\text{conn})}(0)$. The relative error of $\sigma^{(\text{conn})}$ compared to the numerical solution is less than 1.75% for all values of Pe and ϵ , and it becomes negligibly small at high and low Pe for all ϵ .

boundary, Γ , by smoothly connecting $\sigma^{(\text{hi})}$ and $\sigma^{(\text{lo})}$. The dependence of the ux on Pe can be described heuristically by a formula of the form

$$\sigma^{(\text{conn})}(\epsilon; \text{Pe}) = \sigma^{(\text{hi})}(\epsilon; \text{Pe}) U(\epsilon; \text{Pe} = P_0) + \sigma^{(\text{lo})}(\epsilon; \text{Pe}) [1 - U(\epsilon; \text{Pe} = P_0)]; \quad (6.1)$$

for the entire range of Pe; $U(\epsilon)$ is a family of smooth functions defined for $\epsilon = \text{Pe} = P_0 > 0$ that at least satisfy the conditions

$$\lim_{\epsilon \rightarrow 0^+} U(\epsilon) = 0; \quad \lim_{\epsilon \rightarrow +1} U(\epsilon) = 1; \quad (6.2)$$

A simple choice for the step-like function, U , which yields a rather accurate formula for $\sigma^{(\text{conn})}$, is

$$U(\epsilon; \epsilon_0) = e^{1 - (\epsilon/\epsilon_0)^2}; \quad \epsilon_0 > 0; \quad (6.3)$$

We note that there are two free parameters in (6.3) with $\epsilon = \text{Pe} = P_0$: ϵ_0 and P_0 . The parameter P_0 corresponds to a value of Pe in the region of overlap of formulae (4.16) and (5.24); in principle, P_0 may depend on the local coordinate, which is ϵ for the unit circle. The parameter ϵ_0 determines the steepness of the curve $U(\epsilon)$ near $\epsilon = 1$.

We find that a good fit with the numerical solution is achieved for $\epsilon_0 = 2$ and $P_0 = 1/6$, as shown in Fig. 11 where $\sigma^{(\text{conn})}(\epsilon)$ is plotted versus Pe for $\epsilon = \pi$ (upstream ux) and $\epsilon = 0$ (downstream ux). The relative error is less than 1.75% for all values of Pe and ϵ . Because we have the exact Green function (2.7), this uniform accuracy also carries over to the solution of the entire concentration field, $c(x; y; \text{Pe})$, obtained from the integral (2.8).

Our analytical approximation also describes an absorber of arbitrary shape obtained by conformal mapping, $z = g(w)$ ($w = e^i$). The ux distribution on the unit circle, $\sigma^{(\text{conn})}(\epsilon)$, is transformed to the new surface using (2.13). Because the ux is proportional to a gradient, it is locally amplified by a factor of $|g'(w)|^{-1}$, which may cause relative errors larger than 1.75% in some locations, e.g. near a cusp, where conformality breaks down ($g'(w) = 0$). For a well behaved univalent mapping, however, the approximation should remain very accurate for all positions, $g(e^i)$ and Pe, so the general BVP may be considered effectively solved.

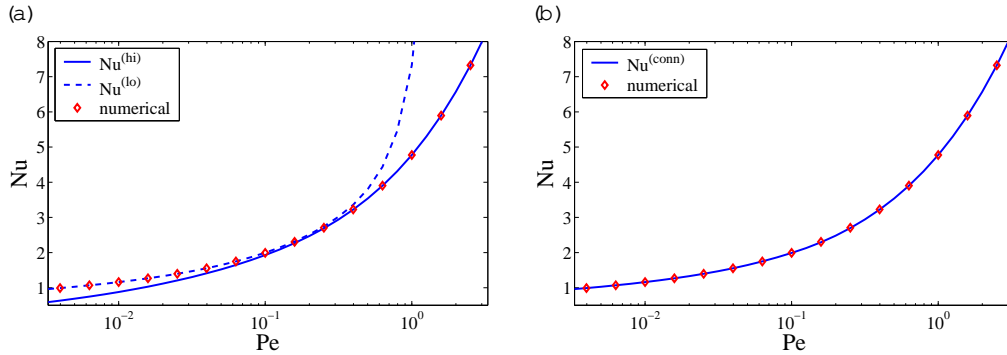


Figure 12. The Nusselt number, Nu , which gives the total flux to the absorber, versus the Peclet number, quantifying the importance of advection compared to diffusion. In (a) the asymptotic expressions (6.5) overlap for $0.1 < Pe < 0.4$. In (b) the analytical connection formula (6.6) compares very well with the "exact" numerical result from Sec. 3. The results hold for absorbers of arbitrary shape, as long as Pe is the renormalized Peclet number, $Pe = A_1 Pe_0$, where A_1 is the conformal radius and Pe_0 is the bare Peclet number for the unit circle.

6.2. The Total Flux to the Absorber

It is straightforward to obtain a uniformly accurate approximation of the Nusselt number by integrating the flux on the unit circle or the finite strip:

$$Nu(Pe) = \int_0^{Z_2} d(x; Pe) = 2 \int_1^{Z_1} dx(x; Pe); \quad (6.4)$$

The leading-order expressions of $Nu(Pe)$ in the high and low Pe limits are thus obtained by integrating (4.15) and (5.23) using integration by parts and the identity $xI_0(x) = [xI_1(x)]'$ (Gradshteyn & Ryzhik; 1980),

$$Nu^{(hi)}(Pe) = \frac{8}{Pe} \left(\frac{r}{Pe} e^{-2Pe} K_0(2Pe) + Pe e^{2Pe} \operatorname{erf}\left(2\sqrt{\frac{Pe}{Pe}}\right) [K_0(2Pe) + K_1(2Pe)] \right); \quad (6.5a)$$

$$Nu^{(lo)}(Pe) = 2 \left[\frac{I_0(Pe)^2}{K_0(Pe=2)} + (Pe)^2 [I_1(Pe)^2 - I_0(Pe)^2] + Pe I_0(Pe) I_1(Pe) \right]; \quad (6.5b)$$

The uniform analytical approximation for $Nu(Pe)$ follows as

$$Nu^{(conn)}(Pe) = Nu^{(hi)}(Pe) e^{-(1 - e^{36Pe^2})} + Nu^{(lo)}(Pe) [1 - e^{-(1 - e^{36Pe^2})}]; \quad (6.6)$$

As shown in Fig. 12, this analytical result is quite accurate over the entire range of Peclet numbers, and it becomes exact as $Pe \rightarrow 0$ and $Pe \rightarrow 1$. The maximum relative error is found to be 0.53%. We are not aware of any such analytical formula for the complete Nusselt-Peclet relation of a finite absorber.

It may come as a surprise that the same result (6.5) also holds for an absorber of arbitrary shape, obtained by conformal mapping of the unit circle, $z = g(w)$, without any additional error. The reason is that the total flux through any contour is preserved exactly under every conformal mapping of a conformally invariant BVP (Bazant, 2004). When computing Nu from (6.4) for another shape, therefore, one must simply use the renormalized Peclet number, $Pe = A_1 Pe_0$, equal to the conformal radius, A_1 , times the bare Peclet number, Pe_0 , for the unit circle.

7. Conclusion

7.1. Summary of Results

We have performed a detailed study of the BVP (1.3)-(1.5) for a finite absorber of arbitrary cross section in a steady two-dimensional potential flow. Our focus has been the flux profile on the boundary, ϕ , from which the concentration can be obtained everywhere in the plane by convolution with the known Green function. We have explicitly considered several simple cases, notably the canonical problem of uniform flow past a circular cylinder, which can be mapped to arbitrary geometries by conformal mapping, as described in Sec. 2.

In Sec. 3, we presented the first accurate numerical solutions of the BVP, using an efficient, new method. We began by mapping the BVP to the inside of the unit circle in order to work with a bounded domain. We then eliminated some "far-field" singularities (at the origin) using exact asymptotics and applied a spectral method in polar coordinates, with exponential convergence in the number of nodes. We also used an adaptive mesh to deal with boundary layers at very high Peclet numbers. The results, which are illustrated in Figs. 2 and 4, provided reliable tests of our analytical approximations.

In Secs. 4 and 5, we derived distinct asymptotic expansions for the flux on the boundary of the finite strip for high and low Pe , respectively, starting from a well known integral equation in stream line coordinates (Wijnngaarden, 1966), which has been studied extensively in the theory of solidification and freezing in a flowing melt (Maksimov, 1976; Chugunov & Komev, 1986; Komev & Chugunov, 1988; Komev & Mukhamadullina, 1994; Alimov et al., 1994; Alimov et al., 1998; Cummings & Komev, 1999; Cummings et al., 1999). We used some original variations on classical techniques from the theory of singular integral equations, including the Wiener-Hopf method of factorization, to obtain improvements on previous approximations.

Noteworthy features of our expansions for high Pe are: (i) The sums admit closed-form expressions in terms of multiple integrals (4.22), which are straightforward to calculate numerically; (ii) the expansions converge for all distances along the strip for a wide range of Pe , $Pe \gg 0(1)$, where the number of terms increases as Pe decreases; and (iii) for $Pe \gg 10^2$, only the small number of terms in (4.16) can be retained for reasonable accuracy for all distances from the ends of the strip. On the other hand, our asymptotic formula (5.24) for low Pe is accurate for $Pe \gg 10^1$, which renders it possible to have a region where the two expansions overlap.

Therefore, we were able to construct an ad hoc analytical connection formula (6.1), which reproduces our numerical results for the flux to a circular absorber with less than 1.75% relative error for all angles and Peclet numbers, as shown in Fig. 11. We also predicted the $Nu(Pe)$ relation (6.4) with comparable accuracy, as shown in Fig. 12. These results constitute a nearly exact, analytical solution to the BVP.

7.2. On the Remarkable Success of Perturbation Methods

A posteriori, we should try to understand why perturbation methods, which ostensibly require extreme values of Pe , produced a very accurate analytical solution for all values of Pe . We argue that this is a consequence of the basic physics of advection-diffusion, as well as some features of our mathematical techniques.

First of all, our high- Pe approximation, $\phi^{(h)}$, is not the usual asymptotic power series, since we have essentially "summed" parts of it exactly in the Bessel function terms of (4.16). This allows it to be more accurate than a simple power series, presumably extending its validity to somewhat higher Pe . Still, the neglected higher-order terms involve powers of Pe , which become important as Pe gets close to unity.

Physically, we are perturbing around a trivial "similarity solution" for the limit, $Pe \rightarrow 0$, which describes uniform diffusive flux from infinity, $c = \text{constant}$ and $c(r; \theta) \sim 1/\ln r$. As shown in Fig 4 (a) for $Pe = 0.01$, a small amount of fluid flow changes this picture only slightly near the disk, by favoring flux to one side compared to the other. When $Pe = 1$, as in Fig. 4 (b), the region of depleted concentration begins to be swept significantly downstream by the flow. This causes the low- Pe approximation to break down near the rear stagnation point, while remaining fairly accurate near the forward stagnation point, as shown in Fig. 9.

The high- Pe approximation is derived by perturbing around the similarity solution (2.16) for an absorbing circular rim on an absorbing flat plate (Bazant, 2004). In this advection-dominated regime, there is a thin diffusion layer of width, $O(1/\sqrt{Pe})$, around the disk, as shown in Fig 4 (c), which provides the first term in the approximation (5.24). The asymptotic corrections in Sec. 4 are obtained by effectively removing the "false plate" from the similarity solution in the wake of the disk.

To understand the influence of the wake region in simple terms, consider the Green function (2.7), which has the asymptotic form

$$G(x; y) \sim \frac{e^{-Pe(x-r)}}{8\sqrt{Pe}} \quad \text{as } r = \sqrt{x^2 + y^2} \rightarrow 1 : \quad (7.1)$$

The Green function decays exponentially at the scale of Pe in all directions, except precisely downstream, where it is long-ranged: $G(x; 0) \sim \frac{1}{8\sqrt{Pe}} e^{-Pe x}$ as $x \rightarrow 1$ for $y = 0$. Therefore, all corrections to the leading-order similarity solution (2.16) decay exponentially upstream beyond an $O(Pe)$ distance from the rear stagnation point. Our high- Pe approximation, $G^{(h)}$, in (4.16) captures the first such correction, which is needed for uniform accuracy over the disk. Further corrections are $O(e^{-4Pe})$, as is clear from the formulae (4.23).

The fact that the approximation breaks down when e^{4Pe} , rather than Pe , gets close to unity explains the fortuitous accuracy of $G^{(h)}$ down to $Pe = 0.1$. Higher-order terms further extend the region of accuracy by orders of magnitude, e.g. to $Pe = O(10^{-3})$ for negative terms, as shown in Fig. 7. Because the approximation is valid for a wide range of Pe that would not be considered "high", it overlaps with the low- Pe approximation and enables a nearly exact solution to the BVP.

7.3. Some Directions for Future Work

The analytical treatment on the basis of an integral equation essentially avoids the complications of boundary-layer theory applied directly to the BVP (Hinch, 1991). In that sense, it resembles renormalization-group (RG) methods for PDEs (Goldenfeld, 1992; Chen, 1996), which provide a general means of deriving asymptotic expansions in place of traditional problem-specific singular-perturbation methods. An attractive feature of RG methods is that they promise to produce globally valid approximations directly, without the need to combine distinct overlapping expansions, as we have done. It would be interesting to see if this could possibly be accomplished for our BVP, and, if so, whether the resulting approximations are any simpler or more accurate than ours. We leave this as an open challenge to RG aficionados.

From the point of view of mathematical methods, another interesting observation is that the BVP (1.3)-(1.5) can be formulated in analogous way to the problem of wave scattering by a finite strip (Meyers, 1965) in acoustics or electromagnetics, which has some variants with other geometries such as the scattering by a broken corner (Meyers, 1984). Such problems, where the requisite PDEs are or can be reduced to Helmholtz-type equations by simple transformations, can be described alternatively by finite sets of

nonlinear ODEs in which the length of the strip, or the Peclet number Pe in the present case, is the independent variable. The underlying method is an improvement over Latta's method (Latta, 1956) for the solution of a class of singular integral equations via their exact conversion to ODEs.

Another technical question is how to place the method of high- Pe expansion pursued in Sec. 4 on a more mathematical ground. To address this issue, one of us has developed an equivalent approach based on a generalization of the Wiener-Hopf technique applied to the BVP in the Fourier domain, which yields the same results as the iteration scheme of Sec. 4 (Argetis, 2004). Since the Wiener-Hopf method is well known in this context for a semi-infinite strip (Carrier et al., 1983), it is perhaps interesting to ask how the method might be extended for the present case of a finite strip, or perhaps more general situations, such as multiple strips.

An exciting physical application of our results is to new phenomena of advection-diffusion-limited pattern formation (Bazant et al., 2003). In the stochastic case of ADLA, the probability measure for adding particles on a growing aggregate in the z plane is given by the flux to the unit disk for the same problem in the w plane,

$$p(z;t) dz = p(w;t) d w / w (; Pe(t)); \quad (7.2)$$

where the renormalized Peclet number, $Pe(t) = A_1(t)Pe_0$, is given by the time-dependent conformal radius. Our accurate numerical solution for $w (; Pe)$ has already been used as the growth measure in the simulations of Bazant et al. (2003). Future simulations or mathematical analysis could start from our nearly exact formula, $w^{(conn)}$ from (6.1), which captures the full crossover between diffusion-dominated and advection-dominated dynamical fixed points with increasing $Pe(t)$. Thanks to conformal mapping, our detailed analysis of a simple model problem has surprisingly broad applicability.

Acknowledgments

TMS and MZB would like to thank Ecole Supérieure de Physique et Chimie Industrielles (Laboratoire de Physico-chimie Théorique) for hospitality and partial support. The authors also wish to thank Konstantin Kornev, John Myers, Howard Stone, Jacob White, and Tai-Tsun Wu for references and helpful discussions.

Appendix A. Systematic derivation of the Green function

In this appendix, we derive systematically the appropriate Green function $G(x;y;x^0;y^0)$ for the boundary value problem of (2.3) and (2.4); G satisfies

$$2Pe \frac{\partial G}{\partial x} = \frac{\partial^2 G}{\partial x^2} + \frac{\partial^2 G}{\partial y^2} + (x - x^0) (y - y^0); \quad (A.1)$$

with $G \rightarrow 0$ as $\frac{1}{x^2 + y^2} \rightarrow 0$.

By representing G by the Fourier integral

$$G(x;y;x^0;y^0) = \int_{-1}^1 \int_{-1}^1 \frac{dk_1 dk_2}{(2\pi)^2} e^{ik_1 x + ik_2 y} \mathcal{G}(k_1; k_2; x^0; y^0) \quad (A.2)$$

and using (A.1), we find

$$\mathcal{G}(k_1; k_2; x^0; y^0) = \frac{e^{-ik_1 x^0 - ik_2 y^0}}{k_1^2 + k_2^2 + 2ik_1 Pe}; \quad (A.3)$$

Hence, with the change of variable $k_1^0 = k_1 + iPe$,

$$G(x; y; x^0; y^0) = e^{Pe(x-x^0)} \int_0^{\infty} \int_0^{\infty} \frac{dk_1 dk_2}{(k_1^2 + k_2^2 + Pe^2)^2} \frac{e^{ik_1^0(x-x^0) + ik_2(y-y^0)}}{k_1^2 + k_2^2 + Pe^2} \quad (A 4)$$

By expressing the integrand of (A 4) in polar coordinates, it becomes evident that $e^{Pe(x-x^0)} G$ depends only on the distance $r^0 = \sqrt{(x-x^0)^2 + (y-y^0)^2}$. We thus take $x-x^0 = 0$ for simplicity, carry out the integration over k_2 and find (Bateman, 1981)

$$G(x; y; x^0; y^0) = \frac{1}{4} \int_0^{\infty} dk \frac{e^{-P\sqrt{k^2 + Pe^2}(y-y^0)}}{k^2 + Pe^2} = \frac{1}{2} K_0(Pe|y-y^0|); \quad (A 5)$$

where $\text{Re} \sqrt{k^2 + Pe^2} > 0$; in the last integral we used the change of variable $k = Pe \sinh t$. Thus,

$$G(x; y; x^0; y^0) = \frac{1}{2} e^{Pe(x-x^0)} K_0(Pe \sqrt{(x-x^0)^2 + (y-y^0)^2}); \quad (A 6)$$

Compare with (2.7) where $x^0 = y^0 = 0$.

Appendix B. Invertibility of the Kernel

In this appendix we show that the symmetrized kernel, $K_0(Pe|x-x^0|)$, of the integral equation (2.9) is positive definite. Using the relation

$$K_0(x) = \frac{1}{2} \int_0^{\infty} dt \frac{\cos(xt)}{1+t^2}; \quad (B 1)$$

the kernel is recast to the form

$$\int_0^{\infty} dt \frac{\cos(\xi t) \cos(\xi_0 t) + \sin(\xi t) \sin(\xi_0 t)}{1+t^2}; \quad (B 2)$$

It follows that, for $\xi > 0$,

$$\int_0^{\infty} d\xi \int_0^{\infty} d\xi \int_0^{\infty} dt \frac{\cos(\xi t) \cos(\xi_0 t) + \sin(\xi t) \sin(\xi_0 t)}{1+t^2} f(\xi_0) f(\xi) = \int_0^{\infty} dt \frac{g(t)^2 + h(t)^2}{1+t^2}; \quad (B 3)$$

by which the kernel is positive definite. The functions $g(t)$ and $h(t)$ are real, and given by

$$g(t) + ih(t) = \int_0^{\infty} f(u) e^{iut} du; \quad (B 4)$$

REFERENCES

Acrivos, A. & Taylor, T. D. (1962) Heat mass transfer from single spheres in Stokes flow. *Phys. Fluids* 5, 387-394.

Aleksandrov, V. M. & Belokon, A. V. (1967) Asymptotic solutions of a class of integral equations and its application to contact problems for cylindrical elastic bodies. *J. Appl. Math. Mech. (Prikl. Mat. Mekh.)* 31, 718-724.

Aleksandrov, V. M. & Belokon, A. V. (1968) Asymptotic solutions of a class of integral equations encountered in the investigation of mixed problems of the mathematical physics for regions with cylindrical boundaries. *J. Appl. Math. Mech. (Prikl. Mat. Mekh.)* 32, 402-413.

Aleksandrov, V. M. & Pozharskii, D. A. (1999) An asymptotic method in contact problems. *J. Appl. Math. Mech. (Prikl. Mat. Mekh.)* 63, 283-290.

- Alimov, M. M., Kornev, K. G., & Mukhamadullina, G. L. (1994) The equilibrium shape of an ice-soil body formed by liquid flow past a pair of freezing columns. *J. Appl. Math. Mech. (Prikl. Mat. Mekh.)* 58, 873{888.
- Alimov, M., Kornev, K., & Mukhamadullina, G. (1998) Hysteretic effects in the problems of artificial freezing. *SIAM J. Appl. Math.* 59, 387{410.
- Bateman Manuscript Project (1981) *Higher Transcendental Functions, Vol. II*, edited by A. Erdelyi, p. 82, New York: McGraw-Hill.
- Batchelor, G. K. (1967) *An introduction to fluid dynamics*. Cambridge: Cambridge University Press.
- Bazant, M. Z. (2004) Conformal mapping of some non-harmonic functions in transport theory. To appear in *Proc. Roy. Soc. A*.
- Bazant, M. Z., Choi, J., & Davidovitch, B. (2003) Dynamics of conformal maps for a class of non-Laplacian growth phenomena. *Phys. Rev. Lett.* 91, art. no. 045503.
- Boussinesq, M. J. (1905) Sur le pouvoir refroidissant d'un courant liquide ou gazeux. *J. de Math.* 1, 285-290.
- Brenner, H. (1963) Forced convection heat and mass transfer at small Peclet numbers from a particle of arbitrary shape. *Chem. Eng. Sci.* 18, 109{122.
- Burgers, J. M. (1948) A mathematical model illustrating the theory of turbulence. *Adv. Appl. Mech.* 1, 171{199.
- Carleman, T. (1922) Über die Abelsche Integralgleichung mit konstanten Integrationsgrenzen. *Math. Zeitschrift* 15, 111{120.
- Carrier, G., Krook, M., & Pearson, C. E. (1983) *Functions of a complex variable*. Ithaca, New York: Hod Books, Chaps. 2, 5 and 8.
- Chen, L. Y., Goldenfeld, N. D., & Oono, Y. (1996) The renormalization group and singular perturbations: multiple scales, boundary layers and reductive perturbation theory. *Phys. Rev. E* 54, 376{394.
- Chugunov, V. A. & Kornev, K. G. (1986) Dynamics of ice-rock barriers under conditions of freezing of filtering rocks. *J. Eng. Phys. (Inzh.-Fiz. Zh.)* 51, 981{986.
- Cummings, L. J. & Kornev, K. (1999) Evolution of a crystallisation front in forced hydrodynamic flow—some explicit solutions. *Physica D* 127, 33{47.
- Cummings, L. M., Hohlov, Y. E., Howison, S. D., & Kornev, K. (1999) Two-dimensional solidification and melting in potential flows. *J. Fluid Mech.* 378, 1{18.
- Eames, I. & Bush, J. W. M. (1999) Long dispersion by bodies fixed in a potential flow. *Proc. Roy. Soc. A* 455, 3665{3686.
- Galina, L. A. (1945) Unsteady filtration with a free surface. *Dokl. Akad. Nauk. S.S.S.R.* 47, 246{249 (in Russian).
- Goldenfeld, N. (1992) *Lectures on Phase Transitions and the Renormalization Group*. Reading, Massachusetts: Perseus Books.
- Gradshcheyn, I. S. & Ryzhik, I. M. (1980) *Tables of integrals, series, and products*. New York: Academic Press.
- Hinch, E. J. (1991) *Perturbation Methods*. Cambridge, UK: Cambridge University Press.
- Howison, S. D. (1992) Complex variable methods in Hele-Shaw moving boundary problems. *Euro. J. Appl. Math.* 3, 209{224.
- Hunt, J. C. R. & Eames, I. (2002) The disappearance of laminar and turbulent wakes in complex flows. *J. Fluid Mech.* 457, 111{132.
- Koplik, J., Redner, S., & Hinch, E. J. (1994) Tracer dispersion in planar multipole flows. *Phys. Rev. E* 50, 4650{4667.
- Kornev, K. G. & Chugunov, V. A. (1988) Determination of the equilibrium shape of the bodies formed during the solidification of filtering flow. *J. Appl. Math. Mech. (Prikl. Mat. Mekh.)* 52, 773{778.
- Kornev, K. & Mukhamadullina, G. (1994) Mathematical theory of freezing for flow in porous media. *Proc. Roy. Soc. London A* 447, 281{297.
- Rein, M. G. (1962) Integral equations on a half line with kernel depending upon the difference of the arguments. *Am. Math. Transl.* 22, 163{288.
- Latta, G. E. (1956) The solution of a class of integral equations. *Rat. Mech. Anal.* 5, 821{831.

- Leal, G. (1992) *Laminar flow and convective transport processes*. New York: Butterworth-Heinemann.
- Magar, V., Goto, T. & Pedley, T. J. (2003) Nutrient uptake by a self-propelled steady squimmer. *Quart. J. Mech. Appl. Math.* 56 (1), 65–91.
- Maksimov, V. A. (1976) On the determination of the shape of bodies formed by solidification of the fluid phase of the stream. *J. Appl. Math. Mech. (Prikl. Mat. Mekh.)* 40, 264{272.
- Margetis, D. (2004) An iteration scheme by the Wiener-Hopf method for a problem in advection-diffusion, preprint.
- Morgan, M. & Bejan, A. (1994) Heatline visualization of forced convection in porous media. *Int. J. Heat Fluid Flow* 36, 42{47.
- Muskhlishvili, N. I. (1992) *Singular Integral Equations*. New York: Dover. (Based on the second Russian edition of 1946.)
- Myers, J. M. (1965) Wave scattering and the geometry of a strip. *J. Math. Phys.* 6, 1839{1846.
- Myers, J. M. (1984) Derivation of a matrix Painlevé equation germane to wave scattering by a broken corner. *Physica D*, 11, 51{89.
- Noble, B. (1988) *Methods based on the Wiener-Hopf technique for the solution of partial differential equations*. New York: Chelsea (2nd Ed.).
- Pearson, C. E. (1957) On the finite strip problem. *Quart. Appl. Math.* XV, 203{208.
- Polubarinova-Kochina, P. Ya. (1945) *Dokl. Akad. Nauk. S.S.S.R.* 47, 254{257 (in Russian).
- Protsenko, V. S. & Rvachev, V. L. Plate in the form of an infinite strip on an elastic half-space. *J. Appl. Math. Mech. (Prikl. Mat. Mekh.)* 40, 273{280.
- Rvachev, V. L. (1956) The pressure on an elastic half-space of a stamp in the form of a strip in a plane. *Prikl. Mat. Mekh.* 20, 163{179 (In Russian).
- Stakgold, I. (1998) *Green's functions and boundary value problems*, second edition. New York: Wiley.
- Titchmarsh, E. C. (1948) *Introduction to the theory of Fourier integrals*, third edition. Oxford: Clarendon Press.
- Trefethen, L. N. (1986) *Numerical conformal mapping*. Amsterdam: North Holland.
- Trefethen, L. N. (2000) *Spectral methods in Matlab*. Philadelphia: Society for Industrial and Applied Mathematics.
- Wijnngaarden, L. van (1966) Asymptotic solution of a diffusion problem with mixed boundary conditions. *Proc. Koninkl. Nederl. Akad. Wet.* 69, 263{276.